8-8-2007

# Divergence Model for Measurement of Goos-Hanchen Shift

Jeffrey Frank Gray
*University of New Orleans*

# Divergence Model for Measurement of Goos-Hanchen Shift

A Dissertation

Submitted to the Graduate Faculty of the
University of New Orleans
in partial fulfillment of the
requirements for the degree of

Doctor of Philosophy
In
Engineering and Applied Sciences

By
Jeffrey Frank Gray

B.S Electrical Engineering, University of New Orleans 1984
M.S. Engineering, University of New Orleans 1986

August 2007

# Copyright

# Dedication

This effort is dedicated to my children, William, Jefferson, Juliette, and Annette.

# Acknowledgement

The author would like to acknowledge the support of Dr. Ashok Puri and Dr. Dimitrios Charalampidis for their leadership, direction, and support during all phases of this effort, as well as, technical challenges and guidance. The author would also like to acknowledge the contributions and support of Dr. Abdul Rahman Alsamman for his questions and comments which aided in maintaining the high standards of performance, Dr. Melody Verges for her questions and calm reassuring support, and to Dr. Vesselin Jilkov for his support and technical expertise in the signal processing aspects of this effort. The author would like to thank the Physics department at UNO for the use of equipment and the Electrical Engineering department at UNO for providing laboratory space and other supporting materials.

# Table of Contents

# List of Figures

# Abstract

In this effort a new measurement technique for the lateral Goos-Hanchen shift is developed, analyzed, and demonstrated. The new technique uses classical image formation methods fused with modern detection and analysis methods to achieve higher levels of sensitivity than obtained with prior practice. Central to the effort is a new mathematical model of the dispersion seen at a step shadow when the Goos-Hanchen effect occurs near critical angle for total internal reflection. Image processing techniques are applied to measure the intensity distribution transfer function of a new divergence model of the Goos-Hanchen phenomena providing verification of the model. This effort includes mathematical modeling techniques, analytical derivations of governing equations, numerical verification of models and sensitivities, optical design of apparatus, image processing



Keywords – Goos-Hanchen, total internal reflection, evanescent waves, image processing, Canny filters, sub-pixel, Superresolution.

# Foreword

This project is a combination of disciplines from Engineering and Physics. At the core is the physical problem of the lateral shift of evanescent waves near total internal reflection called the Goos-Hanchen. The engineering problem is that of developing robust methods for measuring the effect to make it a useable technology. The effort has required expertise is areas of wave physics, mathematics, and advanced image processing. The end result is a set of design criteria, imaging methods, and processing techniques to make plane-wave Goos-Hanchen a viable process competitive with current advanced techniques for measurement of refractive index variations.

The principal contributions of this work are a new model for plane wave shift resulting in verified predictions of the quantitative effects caused by source divergence. These effects lead to a new simplified model with minor modifications to the classical equations. The new model provides a new symmetrical response curve for locating critical angle which did not previously exist. The new model also extends into the microscopic region of the response to predict spatial dispersion effects which have not previously been considered. Experimental results have demonstrated the first observations of this dispersion effect.

Because of the difference in science and technology involved in this effort the report is divided into sections related to the areas of study. Chapter one is a background of literature on the subjects of the Goos-Hanchen effect and on the field of sub-pixel edge detection in images. Imaging edge detection methods have never been applied to the Goos-Hanchen effect. All previous measurements in the field have been made by either photographic means or by electronic position detection of laser spots.

Chapter two explores the physical process of the Goos-Hanchen effect and establishes a divergence model for intensity dispersions of incoming collimated plane waves. It also introduces the concept of edge detection as it applies to Goos-Hanchen and derives the mathematical models for dispersion and sensitivity of edge measurement methods.

Chapter three deals with the practical measurement considerations for a modern plane-wave Goos-Hanchen experiment. The convolving effects of various aperture types are explained and graphical presentations are made. The chapter also depicts the symmetry and montonicities which arise when an edge shift approach is applied and briefly discusses the advantages of the edge shift method over prior practice.

Chapter four presents the image processing considerations and methods whereby the edge shift method can be implemented for maximum sensitivity to shift and changes in shift which result from variations in alignment angles and refractive index ratios.

Chapter five presents experimental results and techniques used in confirming the models developed in chapters two and three. Three independent experiments provide data which support the predictions of spatial dispersion, dependence of shift and slope on divergence and angle of incidence, and dependence of maximum shift on beam collimation quality.

Finally, a summary and set of general conclusions are given in chapter six and references are listed at the end of the text.

optimization, and experimental confirmation of predictions.

# 1. Introduction

## *Goos-Hanchen background*

Since the time of Newton[1], it has been conjectured that internal reflection of light at a dielectric-dielectric interface involves a penetration of the rarer media. This conjecture was first experimentally demonstrated by Goos and Hanchen in 1947[2]. Using multiple reflections to amplify the effect they were able to obtain photographic evidence that showed a lateral offset difference between the reflections at a dielectric-metal interface and at an adjacent dielectric-dielectric interface.

Following the work of Goos and Hanchen[2], Artmann[3] proposed a theory of the phenomena in terms of the phase shift occurring under conditions of total internal reflection. By using equations for the known phase shift and substituting them into the Fresnel reflection coefficients he separately derived equations of the lateral shift for both the parallel and perpendicular states of polarizations of an ideal plane wave. Goos and Hanchen then returned to the laboratory and made new measurements that experimentally demonstrated the dependence of shift on polarization,

$$d_{\perp} = \frac{\lambda}{\pi} \frac{\sin(\theta_i)}{\sqrt{\sin^2(\theta_i) - 1/n^2}}, \tag{1-1}$$

$$d_{ll} = d_{\perp} \frac{\sin^2(\theta_c)}{\sin^2(\theta_i) - \cos^2(\theta_i)\sin^2(\theta_c)}, \tag{1-2}$$

where $\lambda$ is the wavelength of the light, $\theta_i$ is the incidence angle and n is the ratio of the refractive index of the denser medium to the rarer medium. There are several physical explanations for the effect. The simplest to understand is the existence of an evanescent wave in

the optically rarer media. The solution of Maxwell's equations at a dielectric-dielectric boundary yields a wave in the rarer media whose amplitude decreases exponentially with distance from the interface. Energy is transmitted parallel to the interface surface but no net energy flow normal to the surface. If the angle of incidence is exactly equal to the critical angle of the interface, the evanescent wave travels along the surface and is neither transmitted into the rarer media or re-emergent into the denser media. These conditions require a perfect plane wave and a perfectly flat surface. Because neither condition exists in nature all observable Goos-Hanchen shift measurements are finite.

The physics of these surface waves was explored during the late 19$^{th}$ and early 20$^{th}$ century by numerous authors. A survey of their work and associated references are given by Lotsch[8] in his 1968 work. In particular Lotsch refers to the work of Debye[5] who first treated the concept of a real plane wave as a transversally limited collection of unlimited plane waves of slightly different directions of propagation. This is essentially the model we will use as a starting point for our studies.

The concept that total internal reflection involves penetration and rebound into and from the rarer media was first attributed to a conjecture made by Isaac Newton in his Principia Optic. Newton predicted that the path in the rarer media would be parabolic in shape. The modern acceptance of the conjecture comes from the work of Picht[6] and is based upon the principal of conservation of energy and the mathematical solutions of Maxwell's equations.

In 1967 Agudin[7] showed that the Artman's formulation of the GH shift was mathematically equivalent to solution of the internal reflection problem by the process of Time-Delay scattering. His method involved calculation of the steady state Schrödinger equation using the collision lifetime of a simple wave packet. By applying these methods to the relativistic steady state

solutions of Maxwell's equations, the equations derived are of identical form to Artman's equation and in agreement with the experimental findings of Goos and Hanchen. Agudin found the delay time of the internal reflection and the lateral displacement to be given by equations (1-3) and (1-4) respectively,

$$\Delta t = \frac{\lambda n}{c\pi} \frac{\sin(\theta_i)\tan(\theta_i)}{\sqrt{\sin^2(\theta_i) - \frac{1}{n^2}}} \tag{1-3}$$

$$\Delta x_{ll} = \frac{\lambda}{\pi} \frac{\sin(\theta_i)}{\sqrt{\sin^2(\theta_i) - 1/n^2}}. \tag{1-4}$$

In 1964 Renard[8] derived a more general equation for the GH shift and showed that Artman's equation are unrealistic for critical angles near grazing incidence. By considering the magnitude of the magnetic vector and the time average flux across the surface Renard showed that Artman's equation is an approximation which diverges as the angle of incidence approaches $\pi/2$. Renard traced the error to an approximation in prior work and gave a corrected representation for lateral shifts seen in equation (1-5). Renard's[8] work also discusses the solution of internal reflection for a beam of particles using methods very similar to the later work of Agudin[9],

$$d_{\perp} = \frac{\lambda}{\pi} \frac{\mu \sin(\theta_i)\cos^2(\theta_i)/n}{\mu^2 \cos^2(\theta_i) + \sin^2(\theta_i) - 1/n^2} \frac{1}{\sqrt{\sin^2(\theta_i) - 1/n^2}}. \tag{1-5}$$

Here the same notation as in equation (1-1), the factor of magnetic permeability, $\mu$, is added.

In 1970 Horowitz and Tamir[9] addressed to phenomena related to the Goos-Hanchen effect in detail. These included the shift effect itself, the penetration of the energy into the rarer media, and the experimental observations of a weak trailing illumination well beyond the extents of the normally reflected beam. They addressed inconsistencies in the models when the incidence angle was very close to the critical angle. They reasoned, quite accurately, that the angular

deviation of the beam spread establishes a constant maximum shift value which is strongly dependant on the beam width and they argued that the maximum lateral displacement is proportional to the square root of the beam width. A numerical expression for mean beam shift was derived which predicted a peak displacement above critical angle and displaced from critical angle in proportion to the square root of the beam width. Above this angle the mean shift behavior approaches the classical limit of Artman's equation. A heuristic explanation involves the weighted contributions of components above and below the critical angle. It was in this work that a concept of similarity between Gaussian beams and plane wave behavior is introduced. It was conjectured that the shift phenomena would be similar but not identical for similar angular spreads.

In 1972 de Broglie and Vigier[10] offered a possible interpretation of the Goos-Hanchen shift based upon the assumption of nonzero photon mass. They included derivation of both a transverse solution (T-wave) and a longitudinal solution (L-wave),

$$\delta_{\perp} = -2\tan^{-1}\left(\frac{\sqrt{\sin^2(i) - 1/n^2}}{\cos(i)}\right) \tag{1-6}$$

$$\delta_{ll} = -2\tan^{-1}\left(\frac{\sqrt{\sin^2(i) - 1/n^2}}{\cos(i)/n^2}\right). \tag{1-7}$$

They went on to note that the principal objection was based on the fact that their results depended on the existence of photon mass and not its' magnitude.

In the early 1970s with the availability of lasers, the emphasis on studies of GH shifted from plane waves to Gaussian beams. Antar and Boerner[11] showed that beam shift depended on polarization, refractive index, angle of incidence, and beam width. At this point the emphasis in the literature shifts from collimation angles to beam width. Beam width we must note is directly

related to beam divergence for a Gaussian beam. They further went on to show that a similar shift phenomenon of lateral shift occurs at Brewster's angle for the parallel state of polarization. In our numerical studies we find that although the shift at Brewster's angle is larger than the shift at critical angle by several orders of magnitude, the intensity of reflected light is significantly diminished by the Fresnel reflection coefficients which parabolically approach zero at Brewster's angle. Hence any physical exploitation of this effect would be very difficult.

The shift to Gaussian beams in the 1970s was also undertaken to improve the accuracy of measurements and enhance the attainable shifts. Shift enhancement resulted in large measure to improved collimation and the ability to reduce divergence by spreading and collimating laser beams. The advent of electronic spot position measurement devices enhanced the ability to accurately measure the shifted spots. This required a new model for Gaussian beam behavior at internal reflection and led to the angular spectrum analysis and paraxial approaches.

Tamir and Bertoni[12] showed that the boundary conditions at an internal interface yielded waves with complex propagation constants which they termed complex guided waves or leaky waves. They analytically evaluated the behavior of Gaussian beams of varying width at angles of incidence near the critical angle and showed that the Gaussian beam is split into two Gaussian spots. The location and relative intensity of the two spots depended on the beam width and the alignment angle. They went on to discuss and quantify the behavior of so-called backward leaky structures where the Goos-Hanchen shift is in the negative direction. To quote their conclusions,

"The lateral beam shift is large if the incidence angle is close to a critical angle, for which a phase matching condition exists between the incoming beam and a leaky wave supported by the structure. The beam shifting effect is due to a portion of the incident energy that penetrates into the structure and is guided laterally in the form of a leaky wave field. … In addition to undergoing a lateral displacement, the reflected beam profile undergoes some distortion. …"

Beauregard and Imbert[13] discriminated two angular effects on internal reflection by considering a propagating beam consisting of a non-spherical wavefront, i.e., tangential and sagittal focal lines. This led to the postulate of two measurable shifts: the longitudinal or Goos-Hanchen shift which is measured by bringing the tangential focal line into focus, and the transverse shift which can be measured by bringing the sagittal focal line into focus. They reasoned that all other configurations would only result in a blurred section of the beam. They described the physical process as "boosts" associated with "photons tunneling inside the evanescent wave". They included photographic evidence of the shifts obtained by a 28 and 31 internal reflection optical set-up.

In 1973, Green, Kirby, and Timsit[14] were able to experimentally measure the shift behavior of the mean displacement verifying the earlier predictions of Horowitz and Tamir[9]. Their results clearly showed that maximum mean spot position shift occurred at an angle offset from critical angle and that the behavior of mean shift was slightly asymmetrical about the critical angle. Their experiment used 27 internal reflections through an optical flat to produce shifts which could be measured to wavelength precision.

In 1975, Kozaki and Kimura[15] produced numerical studies of beam path through an inhomogeneous material with a gradient index showing that a gradient index could be used as a steering mechanism. This principle has found widespread use in the fiber optics industry.

Starting with Horowitz and Tamir's[9] introduction of the paraxial approximation, Puri, Pattanayak, and Birman[16,17] studied the use of Goos Hanchen effect in the reflection of light propagating through spatially dispersive semiconductor materials such as CdS and GaAs. In such materials the transmitted beam is a superposition of two partially coupled beams called the

upper and lower polariton branches. Their representation of the mean beam shift is given as follows,

$$X_{jj} = -\frac{1}{2\cos(\theta)}\mathrm{Re}\left\{\frac{A_j^j(\theta) z_j}{1 + A_j^j(\theta)\left[y_j - \delta_j^{1/2}\right]}\right\}, \tag{1-8}$$

where

$$z_j = f^{1/2}\omega_r \exp\left(-i\pi/4 + \gamma_j^2/4\right) D_{-1/2}\left(\gamma_j\right)$$

$$y_j = f^{1/2} \exp\left(-i\pi/4 + \gamma_j^2/4\right) D_{1/2}\left(\gamma_j\right)$$

$$\gamma = \sqrt{2}\left(\frac{ik\omega_r\delta}{2} - \frac{x_r}{\omega_r}\right)$$

$$\delta = \sin(\theta) - \sin(\theta_c)$$

and

$$A_j^j(\theta) \equiv i 2^{1/2} {n_T}^{1/2} \cos^{1/2}[\theta]\left\{\frac{1}{k_0} - \frac{\alpha_R - [i, j, 3-j] - 1}{k_1}\right\}. \tag{1-9}$$

$D_\upsilon(\gamma)$ is the Weber (parabolic cylinder) function or order $\upsilon$ and argument $\gamma$, $\omega_r = (k_0 f)^{-1}$ is the beam width, and $\delta_j = n_j(\sin(\theta_c) - \sin(\theta_c))\sec(\theta)$.

In 1977 Beauregard *et al*[18] showed that strong amplification of the Goos-Hanchen effect could be attained by reflecting through multiple layers of material.

In the same year McGuirk and Carniglia[19] first applied the concept of an angular spectrum representation to the Goos-Hanchen problem. Their results were shown to be consistent with Artman's equation and predicted a nonzero shift at grazing incidence contrary to the findings of Lotsch[4]. The angular spectrum approach represents the divergent propagating beam as an integral of individual angular components over a finite range of angles and specifies that a

maximum angular deviation for centerline exists and that the weighted average of the beam deviation from the centerline vanishes.

Kozaki and Sakurai[20] derived an analytical form based upon arbitrary wavelengths and incidence angles for Gaussian beams in a form very similar to the earlier cited works. Their expression with changes for consistency of symbols is,

$$d = \frac{\lambda}{2\pi} \frac{\sin(\theta_i)}{\sqrt{n^2 \sin^2(\theta_i) - 1}}. \tag{1-10}$$

The leaky wave model was again explored by Tamir[21] in 1985. He studied the behavior of waves in leaky type layered structures. He found that layered configurations could act as waveguides for leaky waves if the angle of incidence fell in the range of high rates of change of the reflectance function. These conditions produced four distinct types of effects, lateral shift, focal shift, angular beam shifts, and modification of the beam waist. He went on to observe that these effects were also seen in beams which had profiles differing from Gaussian in shape.

Up to this point the experimental evidence of the Goos-Hanchen effect was meager, limited to a small number of photographic results. In 1992, Bretenaker, Floch and Dutriaux[22] executed a clever technique for measuring shift by exploiting the different shift seen by the parallel and perpendicular states of polarization. Their rationale was to measure the effect for a single reflection, which had not previously been attained. After spatially separating the two eigenstates they introduced an oscillating knife edge to partially obscure one of the shifted waves and measured the intensity variations as the knife edge oscillated. By careful control of the loss anisotropies they were able to calibrate the device for measuring the differential shift between the eigenstates of the incident beam. They were able to isolate small surface effects and to verify the existing models of the beam shift. They found the peak shift to occur above the critical angle

and that the shift function converged to Artman's classical approximation when the incidence angle exceeded the critical angle by more than the divergence angle of the beam.

In later works, Singh and Nayyar[23] studied the shift function for a magneto-optical interface from an optically denser ferrite material into an optically denser ferrite material. Guther and Kleeman[24, 25] studied the internal grating diffraction for total internal reflection and obtained a 36 um shift for a sinusoidal diffraction grating compared with a 1 um shift for comparable undiffracted internal reflection. In 2002, Berman[26] derived the governing equations for the Goos-Hanchen shift in negative refractive index materials and showed them to laterally mirror the predictions for ordinary refractive materials.

Recently, a different approach has been employed for obtaining lateral shifts. The traditional Goos-Hanchen shift at internal reflection is a photonic process wherein polaritons are carriers of the evanescent wave. This total internal reflection occurs at a dielectric-dielectric interface. A similar and related phenomenon occurs at the interface between dielectric and conductive materials. Under resonance conditions when the thickness of the metal coating satisfies resonance conditions, a phononic wave may propagate in the coating giving rise to the process of Surface Plasmon Resonance. Greatly enhanced beam displacements in both the positive and negative direction can be obtained by carefully designing the metallic surface plasmon resonance structures. This is the subject of work by Yin, Hesselink, Liu, Fang, and Zhang[27].

They followed the work of Bretenaker *et al*[22] with a simple modification to the experimental setup. Instead of using an oscillating knife edge they controlled the state of polarization with and electro-optic polarization modulator and were able to obtain shifts as high as 50 wavelengths for a single reflection using a 45 nm silver film. They found that a critical thickness exists above which the lateral shifts is negative. Shift increased in magnitude as the thickness approached the

critical thickness. In the very recent past, this method has been applied to obtain sensitivities to variation in refractive index as small as $10^{-6}$ in n (refractive index).

### *Alternate measurement options*

Nearly all recent methods[22, 27, and 28] for detecting and measuring the lateral shift phenomena have employed electronic position sensing devices which provide an electronic signal which locates the mean position of the beam. These devices are commercially available and their operation is well understood. It is not clear from the literature how the use of such devices compensates for the skewed shape of the laterally shifted Gaussian beams or whether the skew which theorists have predicted is relevant.

In our work we will return to the classical approach of using monochromatic plane-waves. The quantity we are interested in will be the lateral offset which is visible when the collimated plane-wave is shadowed by a step or slit aperture. We will measure the differential between unshifted portions at a thick internal mirror interface and an open dielectric to air interface. We select a metallic coating for the mirror and insure that the coating thickness is sufficiently thick to avoid surface plasmon resonance effects. This is essentially the setup used by experimenters prior to Gaussian beams with the exception that we will operate on single reflections and seek to magnify the physical shift by controlling the collimation quality of the source. This is an area of physical experimentation which has not previously been explored and we believe it will produce fruitful results.

To measure the shadow shifts we will employ modern image processing technique which can extend our ability to resolve edge positions far beyond the viewable limits on image pixels.

## *Image processing background*

Methods for locating edges in images to resolutions better than single pixels is a widespread field of study. This can be accomplished by many methods including center of gravity method[29,30], least squares template matching[29], local energy approach[31] finite difference of Gaussians[32-37], and moment based edge operators[38,39,40], among many others. When edges are tracked along a transition line the position and angular alignment measurement of the line can be enhanced by statistical methods where the variance is reduced by the reciprocal of the number of samples provided the samples are uncorrelated. In photogrammetry applications where target objects of known size and shape are available, circle and ellipse fitting algorithms are used.

The most common types of edge filters are directional derivative filters. The use of these filters involves the convolution of a finite kernel or filter with a 1-dimensional sample of the image under evaluation. These filter kernels are the image analogues of the finite impulse response (FIR) filters used in signal processing[32]. The filtering process consists of convolving the kernel orthogonal to the direction of desired edge detection. The filter is designed so that its output produces a local maximum or minimum at the position of the edge. The maxima can then be further resolved by various interpolation schemes.

Some of the most common filter kernels are given below. All filters are of odd length with a center element of zero value and many are special cases of the generalized Canny filter[32]. An excellent discussion of the filters and the Canny criteria is given by Demigny[35] from which much of this material is derived.

Sobel

[ 1 0 -1] (1-11)

Difference of Boxes DOB

[1 1 … 1 1 1 0 -1 -1 -1 … -1 -1] (1-12)

Canny

$$h(x) = a_1 e^{\alpha x}\sin(\omega x) + a_2 e^{\alpha x}\cos(\omega x) + a_3 e^{-\alpha x}\sin(\omega x) + a_4 e^{-\alpha x}\cos(\omega x), \text{ for } \quad x<0 \qquad (1\text{-}13)$$

$h(x) = -h(-x)$, for x>0, h(x) =0 for x=0

Deriche

$h(x) = x \cdot e^{-\alpha|x|}$ which is a special form of the Canny filter (1-14)

Shen

$$\begin{aligned} h(x) &= e^{-\alpha x} \qquad x > 0 \\ h(x) &= 0 \qquad\qquad x = 0 \\ h(x) &= e^{\alpha x} \qquad x < 0 \end{aligned} \qquad (1\text{-}15)$$

First derivative of Gaussian (FDOG)

$$h(x) = x \cdot e^{\frac{-x^2}{2a^2}} \qquad (1\text{-}16)$$

In Canny's thesis he presented three criteria for optimal detection of signal transitions such as object edges in images.

A. Good detection or maximization of the signal to noise ratio (SNR) of the filter output superimposed on the background noise of the image.

B. Good localization of the measured edge to the true edge in the field of background noise

C. Low response multiplicity or single maxima of the filter response when applied to the image.

Condition A refers to the relative contrast of the transition from light to dark at the edge compared to the average background noise of the image. The SNR contains two terms; the contrast ratio across the ideal edges, and the background noise level compared to an ideal image.

Condition B refers to the accuracy of a particular method. Odd length filter sequences tend to produce more accurate results if they are antisymmetrical about the center position. Even length sequences produce systematic errors which tend to be antisymmetrical about the half pixel position. Asymmetrical filters produce skew effects on the localization process.

Condition C relates to the multiplicity of local peaks in the filter output which would occur if the floor and plateau of the edge contain notable oscillations in intensity. If this occurs within a window whose width is less than the width of the filter kernel it may be impossible to determine the true edge signature from spurious edge signatures.

The process of applying an edge filter consists of three steps. First, the selected filter is convolved with the image. This is typically done within a region of interest (ROI). The ROI is a user selected section of the image where edges are known to exist. Next a threshold level of filter response is tested for all points in the filter output to resolve the edges to discrete pixels locations. When multiple adjacent positions exceed the threshold value the maximum value position is selected. Then the final step is to apply a sub-pixel interpolation scheme to localize the edge more accurately than a single pixel position.

Interpolation can be done by one of several methods. Some of the most common are the center of gravity method, least squares comparison to an edge template, 1-D cubic interpolation, zero crossings of second derivatives, and the quadratic fit method used in this effort.

All of the filters previously given are first derivative filters and they produce local extrema in the vicinity of leading and trailing edges as seen in figure 1-1.

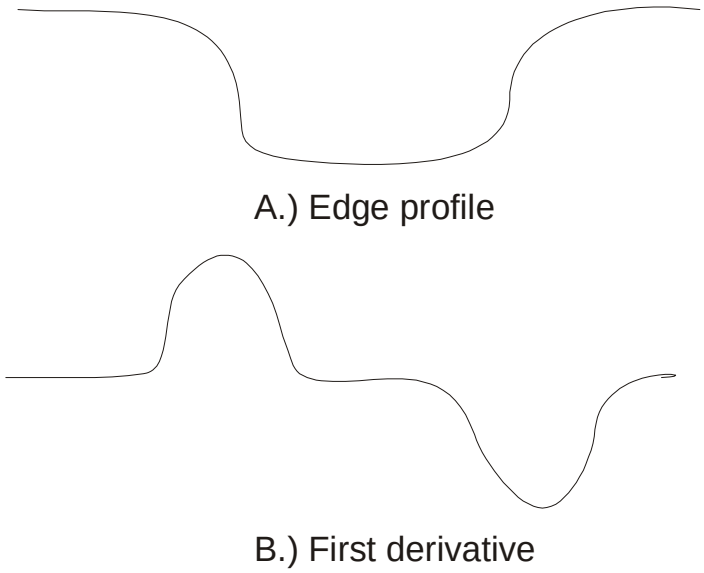


Figure 1-1 – First derivative edge detection process

Quadratic interpolation models the extrema regions of the first derivative as parabolic segments and calculates an interpolated subpixel location for the zero slope position on the parabola based upon the sampled values adjacent to the peak position. The formula for this interpolation can easily be derived from the quadratic formula but have been given by Ohtani and Baba[41]. A clear advantage of this method over center of mass methods is that the quadratic fit can be easily coded into an array processing software language such as the Matrox Imaging Library. An alternate and equivalent form has been given by Li, Young, and Magerl[42].

$$y = a(x - j_0)^2 + b(x - j_0) + c$$

*where*

$$a = \frac{g_{j_0-1} - 2g_{j_0} = g_{j_0+1}}{2}$$

$$b = \frac{g_{j_0+1} + g_{j_0-1}}{2} \qquad (1\text{-}17)$$

$$c = g_{j_0}$$

$$x_{\max} = j_0 - \frac{b}{2a}$$

$$x_{\min} = j_0 + \frac{b}{2a}$$

The localization error given by Ohtani and Baba[41] is .061 pixels to 1 standard deviation.

In our dissertation, the ability to resolve sub-pixel edge position is an enabling technology. We seek only to test various filters and optimize performance to the best attainable level of performance. We satisfy the first of Canny's criteria by optimizing design of our optical apparatus to reduce noise and by integrating multiple images to remove the random noise introduced by the camera's electronics. We satisfy Canny's third criteria by backlighting of high quality targets and minimization of diffraction effects. The second criteria then remains as the design driver for testing various filter configurations.

# 2. The Goos-Hanchen Phenomena[49]

## *Introduction*

In 1947 Goos and Hanchen[2] verified an earlier conjecture by Newton[1] that light beams incident at an internal reflection boundary experienced lateral shifts along the plane of the interface before being reflected. This shift is now known as the Goos-Hanchen shift. The standard equations for calculating the shifts for both parallel and perpendicular states of polarization[43] are functionally dependant on the angle of incidence and the ratio of index of refraction between the two mediums. In the standard form the equations describe the behavior of ideal light sources, however; the nonideal nature of real world sources must be included for proper interpretation of observed results.

The measured Goos Hanchen shift near critical angle was finite[2] but expressions for shift reported in literature diverged near critical angle. A detailed earlier review of theory and experiment was given by Lotsch[4]. Researchers including deBroglie[10], Troup[44], Horowitz and Tamir[9], Puri and Birman[17], and Antar and Boerner[11], among others have proposed methods of approximating the nonideal nature of the phenomena and have developed models for finite Gaussian beam shift near critical angle. The general observation that maximum shift actually occurs slightly off of the critical angle is supported by the Gaussian beam models. Contemporary efforts in GH shift have focused on the shift induced in the TM states of Gaussian beams under plasmon surface resonance[22, 27, and 28].

Our purpose in this dissertation is to investigate a parallel quantitative method which provides a deeper understanding of nonideal plane wave interaction at internal reflection near critical angle. First, we introduce a numerical modeling approach and demonstrate compatibility with

prior science (see figure 1-3 and explanations thereafter). Then we evaluate the resulting dispersion relationships (2-21 generalized to 2-19) which lead to the non-monotonic behavior of the mean shift properties. We find that a new class of measurement methods exists which exploit the edge-shift, or minimum shift, phenomena exhibited along the shadow lines of step apertures. Most prior experimental efforts have relied on detection of mean shift of beam spots and there is near universal agreement that maximum mean shift occurs at angles slightly offset from critical angle. The new method laid down in this effort identifies an alternate measurable parameter, the aperture edge shift (2-10), which exhibits maximum deflection at critical angle and maximum sensitivity to angular alignment at the critical angle (2-30). The edge shift function (2-15) is monotonic on either side of the critical angle as is its derivative (2-28).

Such behavior is well suited for precise location of critical angle leading to improved resolution in refractive index measurement. This treatment leads to a mathematical formulation showing that control of beam divergence is a principal limiting factor in enhancing Goos-Hanchen shift near critical angle. This chapter also defines criteria for comparing observed beam shift data with theoretical results. The problem requires that we examine the definition of beam shift and discriminate the classical method of edge detection from the mean shift predictions of the equations.

In this chapter uniform divergence model is used as an approximation in description of the non-ideal nature of a real optical source. Many additional factors e.g., irregularities in aperture, non-uniform source distribution, alignment and scattering among others contribute towards real source anomalies.

Thus real optical source is not limited by only uniformly divergent waves. However, by establishing a standard plane-wave source based upon well controlled beam qualities and

divergences we can set a nominal baseline from which in principle, other source deviations can be extracted by interpreting measured deviations from the nominal response curves.

The present work is motivated by both fundamental and practical considerations. Measurement of refractive index variation has strong potential for diagnosis of efficiency in liquid and gas mixing applications, measurement of homogeneity of solid materials and noninvasive contamination testing. In addition the resulting form also provides diagnostic information that may be useful in a broad range of physical applications including optical source collimation and alignment considerations.

## *The Divergence Approach*

All natural and manmade sources emanate from finite size sources and possess some form of natural divergence. Our goal is to model the natural divergence and derive a Green's function for the distributed Goos-Hanchen effect over the cone of divergence that results from consideration of the finite dimensions of the source.

Consider a plane wave incident on an internal reflection surface with a uniform cone of divergence as shown in figure 2-1. To define the general impulse response that occurs at each individual point of the reflection interface, we must first determine the amount and direction of light arriving at the interface. This is the collimation of the wave and we generalize our definition to that of a uniform circular source with finite dimensions at some distance from the interface. Without loss of generalization we can reflect the incoming convergent cone of light to an outgoing diverging cone. If we define the Y-Z plane as the interface plane, we can deconstruct the incoming beam into two vectors, one vector along the mean direction of the wave and a second vector representing the divergence cone aligned to the z-axis. This provides an

elegant dot-product representation of the divergent wave that can be applied directly to the Goos-Hanchen shift equation.

When this model is applied to the shift equations, we find a variation in the individual component responses of the wave, depending on the degree to which the divergence causes the incidence angles of the individual components to deviate from critical angle. Only a small portion sees significant shifts and virtually none of the beam sees the infinite shift that occurs along the singularity line.

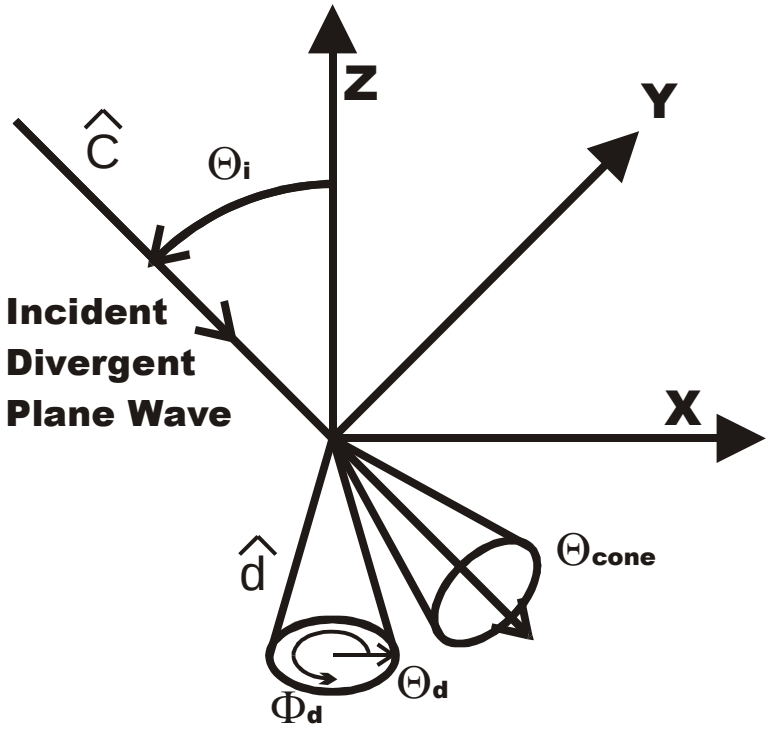


Figure 2-1 – Divergence Geometry

Uniform divergence means that wave propagation is uniform within a fixed theta/phi cone of divergence. At any point in the beam, light rays propagate within a small uniform angular deviation from the beam propagation vector. If we choose the z-axis normal to the optical interface plane then the divergence cone can be expressed in vector form as $\hat{d}$ and the incident

plane wave can be expressed as $\hat{c}$ by the following vectors, where phi and theta are the polar angles defining the divergence cone.

$$\begin{aligned}\hat{d} &= \left(\sin(\theta_d)\sin(\phi_d), \sin(\theta_d)\cos(\phi_d), -\cos(\theta_d)\right) \\ \hat{c} &= \left(\sin(\theta_i), 0, -\cos(\theta_i)\right)\end{aligned} \tag{2-1}$$

Also $\cos(\theta_r) = \left(\hat{c} \cdot \hat{d}\right)$

This represents the incidence angle of each component within the divergence cone. By recasting the Goos-Hanchen equation into a cosine form we can directly apply the dot product and obtain a representation of the shift equation in terms of the divergence cone angles,

$D_\perp = \frac{\lambda}{\pi} \cdot \frac{\sin(\theta_c)}{\sqrt{\sin^2(\theta_c) - \sin^2(\theta_i)}}$ , becomes $D_\perp = \frac{\lambda}{\pi} \cdot \frac{\sin(\theta_c)}{\sqrt{\cos^2(\theta_r) - \cos^2(\theta_c)}}$.

The incidence subscript (i) here is changed to a refraction subscript (r) indicating we have shifted from a plane wave model to a divergence model.

Expanding the dot product, $\cos(\theta_r) = \left(\hat{c} \cdot \hat{d}\right)$, we obtain,

$$\cos(\theta_r) = \sin(\theta_c + \delta)\sin(\theta_d)\sin(\phi_d) + \cos(\theta_c + \delta)\cos(\theta_d). \tag{2-2}$$

The delta angle ( $\delta = \theta_i - \theta_c$ ) in equation (2-2) allows for deviation of the incident angle around the critical angle.

In this uniform divergence model the Goos-Hanchen equation singularities lie along a theta-phi contour in the divergence cone that can be found from (2-2) for all values of delta less than the divergence of the beam. The resulting contours as a function of δ are concentric long radius (compared to $\theta_d$) circular arcs. A simplified representation is given as follows,

$$\sin(\phi_d) = \frac{\cos(\theta_r) - \cos(\theta_c + \delta)\cos(\theta_d)}{\sin(\theta_c + \delta)\sin(\theta_d)}, \tag{2-3}$$

where $\theta_r = \theta_c$ near the critical angle.

***Analytical / Numerical Results***

The shift function plotted as height over the circle of the divergence cone is shown in figure 2-2 with a delta angle of 1/2 of the divergence angle of the beam. The singularity contour is truncated for clarity and overlaid for labeling.

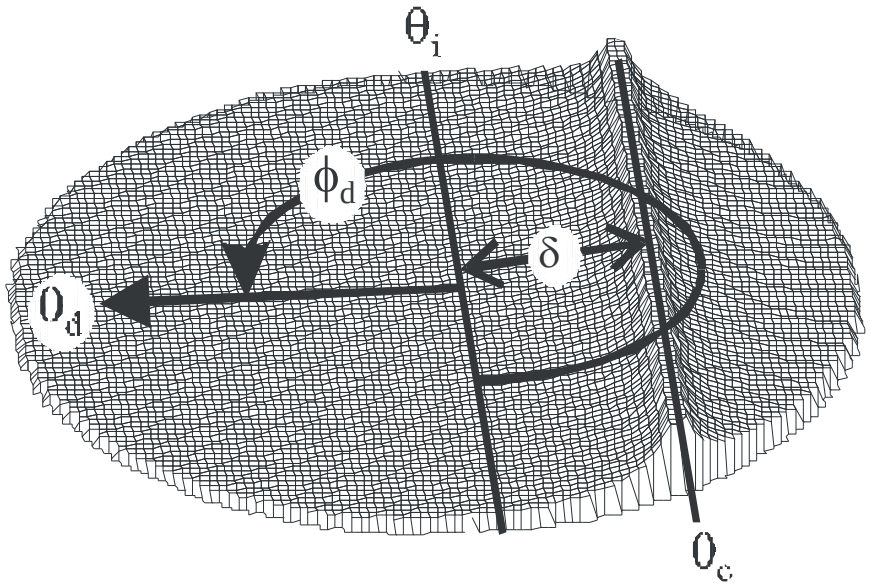


Figure 2-2 - Goos-Hanchen Shift Distributions over the Cone of Divergence

Mean beam offset can now be calculated from standard centroid techniques in a theta, phi polar representation over the cone of divergence,

$$D_{mean} = \frac{\iint D_{\perp}(\theta_d, \phi_d)\theta_d \, d\theta_d \, d\phi_d}{\iint \theta_d \, d\theta_d \, d\phi_d}. \qquad (2\text{-}4)$$

The integral is further divided into two separate components, the portions of the beam incident above and below the critical angle. Above the critical angle totally reflection occurs, but below the critical angle the Fresnel reflectance coefficients that drop off rapidly must be applied. The

observed shift will be a combination of the intensity contributions from the two components. The reflection coefficient drop-off in the region below critical angle is observed to cause asymmetry in the mean displacement versus delta angle curves.

Figure 2-3 shows the relationships between the delta angle, the beam divergence and the predicted mean shifts of the beam by the model. The shift curve is nearly flat at critical angle and does not substantially decline until delta approaches the divergence angle.

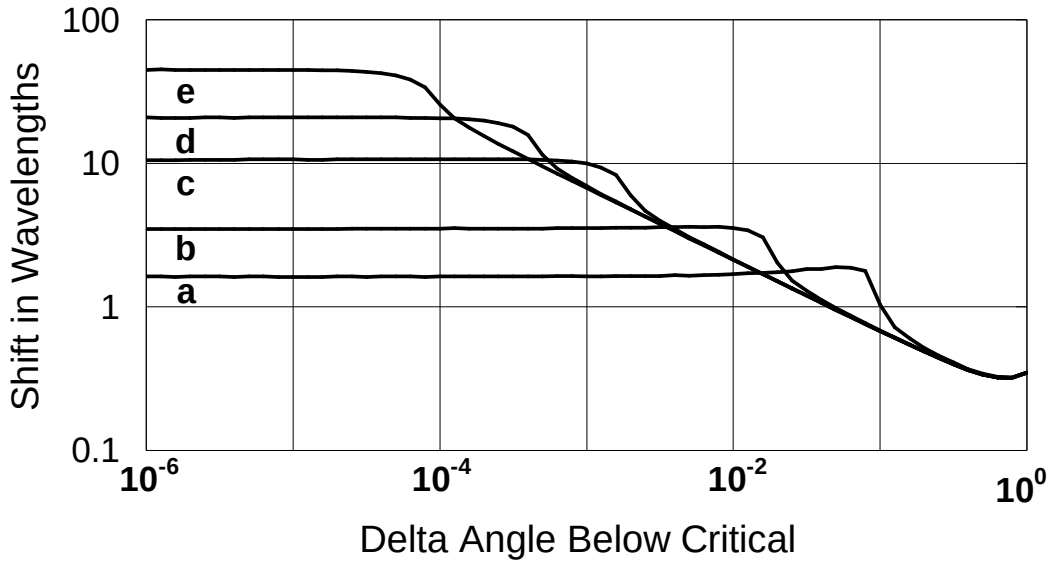


Figure 2-3 – Mean Shift vs. Delta Angle and Divergence Below Critical Angle. Lines a, b, c, d, and e correspond to divergences of .01, .002, .0002, .0005, and .0001 respectively. The common convergence line corresponds to Artman's inverse square root equation.

At small divergences, the shift rolls off slowly below critical angle and drops exponentially when delta exceeds the divergence angle. At larger divergences the shift will rise slowly and reach maximum near the divergence angle before dropping exponentially. This case is for the perpendicular polarization at incidence angles below critical. For delta angles larger than the

divergence angle, the mean shift response asymptotically approaches the classical equation of Artmann's ideal response curves.

It is worth noting that similar finite beam shifts at critical angle have been reported in paraxial, or angular spectrum, approximation[12, 16]. The conjecture of Horowitz and Tamir[9] that nongaussian wave behavior for mean shift will be similar but not identical to Gaussian beam behavior is supported by our numerical models.

The equation for mean beam shift (2-4) can be misleading when used in interpretation of experimental results. Due to the microscopic size and asymmetric shape of the dominant shift effect, mean displacement is difficult to measure accurately with imaging methods. Traditional edge detection methods typically locate the maximum slope of the image intensity profile at the edge. In the divergence model the maximum slope occurs at the leading edge of the shifted image, permitting a direct calculation of the minimum shift the divergence cone sees as follows,

$$D_{\perp edge} = \frac{\lambda}{\pi} \cdot \frac{\sin(\theta_c)}{\sqrt{\left|\sin^2(\theta_{\max}) - \sin^2(\theta_c)\right|}}. \qquad (2\text{-}5)$$

$\theta_{\max} - \theta_c$ is the maximum deviation of the divergence cone from the critical angle and establishes the minimum shift.

The impulse response shift is found by numerical methods as a histogram of the Goos-Hanchen shift over the cone of divergence at a single point. This will define the light wave behavior for a single point input. Typically we would describe this in terms of a point-spread function. But since the shift is most readily seen near linear edges, the logical extension to a line spread function is more appropriate for our purposes.

This is because in real applications the off-axis or longitudinal shifts for small divergences relative to the angle of incidence are negligible in comparison to the lateral shift. Exceptions to

this rule must be considered when the divergence angle becomes a significant percentage (>5%) of the angle of incidence.

The resulting Green's function can then be convolved over the plane wave incidence region (i.e., over slit width) to provide an estimate of the output intensity profile for total beam behavior near lateral edges.

Figure 2-4 shows a typical line spread function for a .01 radian divergence beam. The sharp leading edge of the curve that is the most recognizable feature of the graph from an image processing perspective, locates the minimum displacement given in equation (2-5).

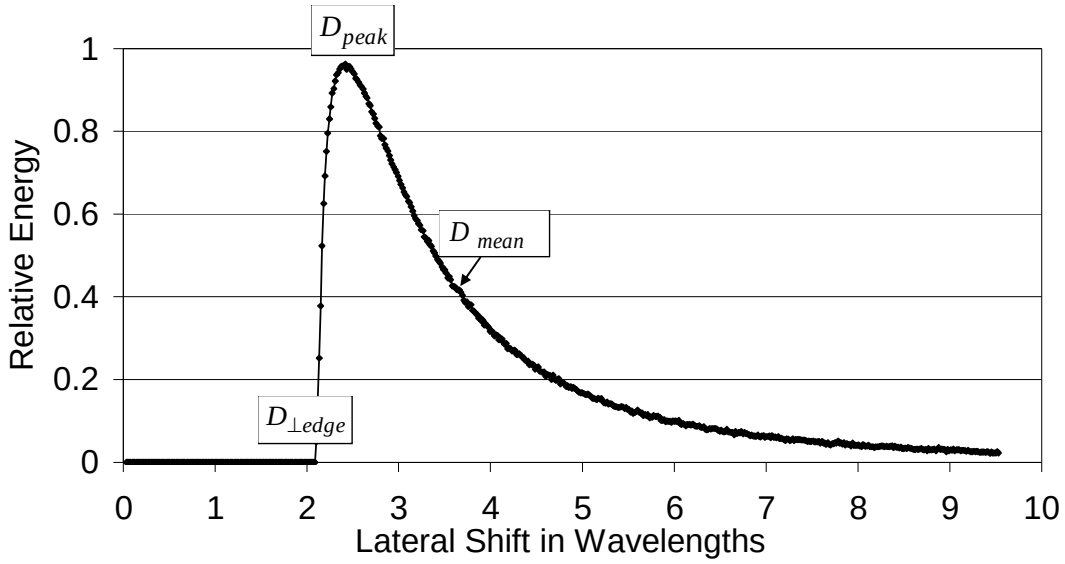


Figure 2-4 – Goos-Hanchen Line Spread Function for δ=0

A nearly exact expression for the line spread function can be derived from the classical theory. Starting with Artman's shift equation we seek to separate the effects of alignment error from the effects of refractive index which determine the critical angle,

$$D_{\perp} = \frac{\lambda}{\pi} * \frac{\sin(\theta_i)}{\sqrt{\sin^2(\theta_i) - \sin^2(\theta_c)}} \qquad (2\text{-}6)$$

$$D_{\perp} = \frac{\lambda}{\pi} * \frac{\sin(\theta_i)}{\sqrt{\sin(\theta_i) + \sin(\theta_c)}\sqrt{\sin(\theta_i) - \sin(\theta_c)}}. \tag{2-7}$$

We separate, regroup, and recollect terms to produce equation (2-8)

$$D_{\perp} = \frac{\lambda}{\pi} * \frac{\sin(\theta_i)}{\sqrt{2\sin\left(\theta_i + \frac{\delta}{2}\right)\cos\left(\theta_i + \frac{\delta}{2}\right)}\sqrt{\sin(\delta)}}. \tag{2-8}$$

If $\theta_i >> \delta$ *and* $\delta << 1$ then (2-8) can be approximated by

$$D_{\perp} = \frac{\lambda}{\pi} \frac{1}{\sqrt{2\cot(\theta_i)}\sqrt{\delta}}. \tag{2-9}$$

In the limit as $\delta \to 0$, $D_{\perp} \to \infty$.

The dependence of shift on $\delta$ is now partially separated

For a distributed source divergence represented by the circle above, the output shift becomes a function of position (d) in the cone of divergence. The Jacobian which relates the input d-space to the output D⊥-space becomes the derivative of the shift function,

$$D_{\perp} = \frac{\lambda}{\pi} \frac{1}{\sqrt{2\cot(\theta_i)}\sqrt{\sin|\delta - d|}}$$

$$\frac{\Delta D_{\perp}}{\Delta d} = \frac{\lambda}{\pi} \frac{\cos|\delta - d|}{\sqrt{2\cot(\theta_i)}\sqrt{(\sin|\delta - d|)^3}} (m/rad) \tag{2-10}$$

where $-\theta_d \le d \le \theta_d$.

The contours of constant angle of incidence can be graphically represented in the space of the divergence cone. Although they are in general circular arcs, they can be approximated as vertical line segments for all divergences of practical interest. This is because the actual arc

length varies from the chordal length by the approximation $\sin(x) \cong x$, where x is the divergence of the beam. Practical apparatus for exploiting this effect will use divergences of less than .01 radians and the errors will be on the order of $10^{-6}$. With this approximation in mind we construct a graphical representation of the segments of uniform shift which allows us to cast an intensity shift equation in the d or divergence space.

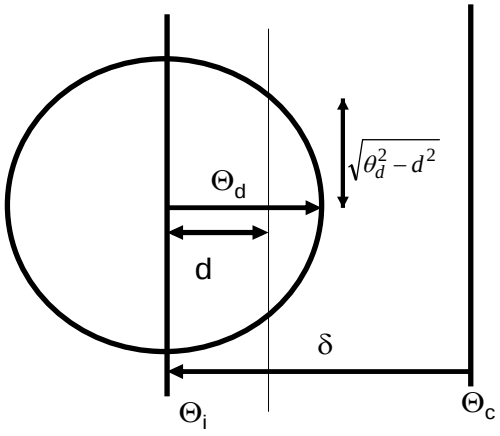


Figure 2-5 – Divergence cone geometry

The total energy in a vertical section of the divergence cone is simply the integral of the intensity in the vertical direction.

We divide by the Jacobian (2-10) to obtain the intensity distribution as a function of shift position. For a uniform circular spot this becomes,

$$I(D_\perp) = \frac{2I_0}{\pi\theta_d^2}\sqrt{\theta_d^2 - d^2}\,\Delta d \Big/ \Delta D_\perp \tag{2-11}$$

$$I(D_\perp) = \frac{2I_0}{\lambda\theta_d^2}\sqrt{\theta_d^2 - d^2}\,\sqrt{2\cot(\theta_i)}\,\frac{\sqrt{\left(\sin|\delta - d|\right)^3}}{\cos(\delta - d)}\,. \tag{2-12}$$

This equation is now the shift distribution in the input d-space. To describe the intensity distribution in output or shifted space we must convert the d-variable to a D⊥-variable. First we recast Artman's equation for direct substitution,

$$d = \delta - \lambda^2 / \pi^2 D_\perp^2 2\cot(\theta_i) \ ,$$

$$\sqrt{\theta_d^2 - d^2} = \sqrt{\theta_d^2 - \left(\delta - \lambda^2 / \pi^2 D_\perp^2 2\cot(\theta_i)\right)^2}$$

$$= \sqrt{\theta_d^2 - \delta^2 + \frac{\delta * \lambda^2}{\pi^2 D_\perp^2 \cot(\theta_i)} - \frac{\lambda^4}{\pi^4 D_\perp^4 4\cot^2(\theta_i)}} \ , \qquad (2\text{-}13)$$

$$\theta_d^2 - d^2 = \theta_d^2 - \delta^2 + \frac{2\delta(\delta + \theta_d) D_{\perp edge}{}^2}{D_\perp^2} - \frac{D_{\perp edge}{}^4 (\delta + \theta_d)^2}{D_\perp^4} \ , \qquad (2\text{-}14)$$

where

$$D_{\perp edge} = \frac{\lambda}{\pi} * \frac{1}{\sqrt{2\cot(\theta_i)}\sqrt{\sin(\theta_d + \delta)}} \ . \qquad (2\text{-}15)$$

From (2-5) and (2-10),

$$\frac{D_{\perp edge}}{D_\perp} = \frac{\sqrt{\sin(\delta - d)}}{\sqrt{\sin(\theta_d + \delta)}} ,$$

$$\left(\frac{D_{\perp edge}}{D_\perp}\right)^3 \sqrt{\sin(\theta_d + \delta)^3} = \sqrt{\sin(\delta - d)^3} \ . \qquad (2\text{-}16)$$

In the limit as $\delta \to 0$ equation 2-13 reduces to

$$\sqrt{\theta_d^2 - d^2} = \theta_d \sqrt{\left(1 - \frac{D_{\perp edge}{}^4}{D_\perp^4}\right)} . \qquad (2\text{-}17)$$

Combining this result with (2-14) and letting $\delta \to 0$ yields,

$$Lim_{\delta \to 0}(I(D_\perp)) = \frac{I_0}{\lambda}\sqrt{\theta_d}\frac{D_{\perp edge}^3}{D_\perp^3}\sqrt{1 - \frac{D_{\perp edge}^4}{D_\perp^4}} \ . \qquad (2\text{-}18)$$

Corrections to this approximation for $\delta \neq 0$ due to the quadratic term in (2-13) can be obtained by altering the powers under the radical to non-integer values. This technique accounts well for the erratic behavior of the function when the alignment angle approaches the divergence angle. This produces the Green's function for shift distributions below divergence angle,

$$I_{LSF} = \frac{I_0}{\lambda \theta_d} \sqrt{2\cot(\theta_i)} \sqrt{(\sin(\theta_d + \delta))^3} \sqrt{\left(\frac{D_{\perp edge}}{x}\right)^a - \left(\frac{D_{\perp edge}}{x}\right)^b} \quad . \qquad (2\text{-}19)$$

$$x \geq D_{\perp edge}$$

To split the leading and trailing components of the shifted wave fronts in the region below divergence the sign of the shift angle δ must be taken into account. This minor adjustment is given in equation (2-19).

In the region where the magnitude of the alignment angle is greater than the magnitude of the divergence angle, equations (2-21) and (2-22) give complete expressions for the shift distribution. For numerical calculations the form of equation (2-15) combined with the positional conversion of (2-13) is best suited for describing the shift distributions. When the shift angle is greater than the divergence angle the impulse response is bounded and the upper limit of D⊥ is given by $D_{\perp edge2}$ given in equation (2-20),

$$D_{\perp edge2} = \frac{\lambda}{\pi} \frac{1}{\sqrt{2\cot(\theta_i)} \sqrt{\sin(\delta - \theta_d)}} \, . \qquad (2\text{-}20)$$

It should be noted for consistency that many of these equations are approximations based upon representing sin(x) as x. This approximation is very accurate when x < .01 radians. The expressions for $\cot(\theta_i)$ is valid when δ is much smaller than $\theta_i$. This approximation breaks down when the source divergence is very large or when the angle of incidence becomes very small. The former case occurs when poorly collimated sources are used. The latter case occurs for

large ratios of refractive index. A final condition occurs near grazing incidence where we must require that $\theta_i + \delta < \pi/2$,

$$I(D_\perp) = \frac{2I_0}{\lambda\theta_d^2}\sqrt{\theta_d^2 - \delta^2 + \frac{\delta\lambda^2}{\pi^2 D_\perp^2 \cot(\theta_i)} - \frac{\lambda^4}{\pi^4 D_\perp^4 4\cot^2(\theta_i)}}\sqrt{2\cot(\theta_i)}\left(\frac{D_{\perp edge}}{D_\perp}\right)^3\sqrt{(\sin(\theta_d+\delta))^3} \quad \forall\delta\,. \quad (2\text{-}21)$$

Or alternately,

$$I(D_\perp) = I_0\frac{\lambda^2}{\pi^3\theta_d^2}\frac{1}{2\cot(\theta_i)}\frac{1}{D_\perp^3}\sqrt{\theta_d^2 - \delta^2 + \frac{\delta\lambda^2}{\pi^2 D_\perp^2 \cot(\theta_i)} - \frac{\lambda^4}{\pi^4 D_\perp^4 4\cot^2(\theta_i)}} \quad \forall\delta\,. \quad (2\text{-}22)$$

(2-21) and (2-22) are both valid for $D_{\perp edge} \le D_\perp \le D_{\perp edge2}$ and the $\cos(\delta - d) \cong 1$ term has been suppressed for notational simplicity. Alternately,

$$I(D_\perp) = \frac{2I_0}{\lambda\theta_d^2}\sqrt{\theta_d^2 - d^2}\sqrt{\cot(\theta_i)}\sqrt{(\delta - d)^3}\,, \quad (2\text{-}23)$$

where $d = \delta - \lambda^2 / \pi^2 D_\perp^2 2\cot(\theta_i)$.

Equation (2-23) is valid for $\theta_i >> \delta \;\; and \;\; \delta << 1$. When $\delta \le \theta_d$ a simpler expression for the line spread function seen in figure 2-4 is given by a closed form approximation (2-24),

$$I_{LSF} = \frac{I_0}{\pi\theta_d}\sqrt{(\sin(\theta_d+\delta))^3}\sqrt{2\cot(\theta_i)}\sqrt{\left(\frac{D_{\perp edge}}{x}\right)^a - \left(\frac{D_{\perp edge}}{x}\right)^b} \quad x \ge D_{\perp edge}\,. \quad (2\text{-}24)$$

The coefficients "a" and "b" are empirically derived; x is the lateral shift value and $D_{\perp edge}$ is found from equation (5). At critical angle the values of "a" and "b" are ~6 and ~10 respectively for the leading components of waves with divergences less than .01 radians. This derives directly from (A12). As delta increases from zero to the divergence angle, the values of "a" and "b" tend to converge towards a value of 8. The analytical form with the harmonic oscillator terms is given in (2-21 0r 2-22). For ease in numerical calculations the approximate form of (2-

24) gives results within 1% for appropriate values of “a” and “b” as verified by numerical modeling.

The line-spread function given in (2-23) and (2-24) and shown in figure 2-4 represents one of the two portions of the complete line spread function. If the beam is incident at the critical angle and the divergence is small enough to minimize the reflectance losses, the leading and trailing shift functions will be nearly identical and the total shift will normalize to the given results. When the incidence angle of beam varies between the critical angle and the divergence angle, the leading and trailing components will be different and the total line spread function will be a sum of the two contributions. For divergences of .01 radians and greater, the reflectance factors in the trailing components become significant and the trailing component graph will be shortened and reduced in overall magnitude. Equation (2-24) is modified to reflect the distinction between the leading and trailing components resulting in equation (2-25) that is the line spread Green’s function for the divergence model when $\delta$ is less than or equal to the divergence angle. The square root of the negative quantity in the trailing component accounts for the phase difference between leading and trailing spots (see figure 2-6),

$$I_{LSF} = \frac{I_0}{\pi\theta_d}\sqrt{(\sin(\theta_d + \delta))^3}\sqrt{2\cot(\theta_i)}\sqrt{\left(\frac{D_{\perp edge}}{x}\right)^{a_L} - \left(\frac{D_{\perp edge}}{x}\right)^{b_L}} + \frac{I_0}{\pi\theta_d}\sqrt{(\sin(\delta - \theta_d))^3}\sqrt{2\cot(\theta_i)}\sqrt{\left(\frac{D_{\perp edge}}{x}\right)^{a_T} - \left(\frac{D_{\perp edge}}{x}\right)^{b_T}} \quad . \quad (2\text{-}25)$$

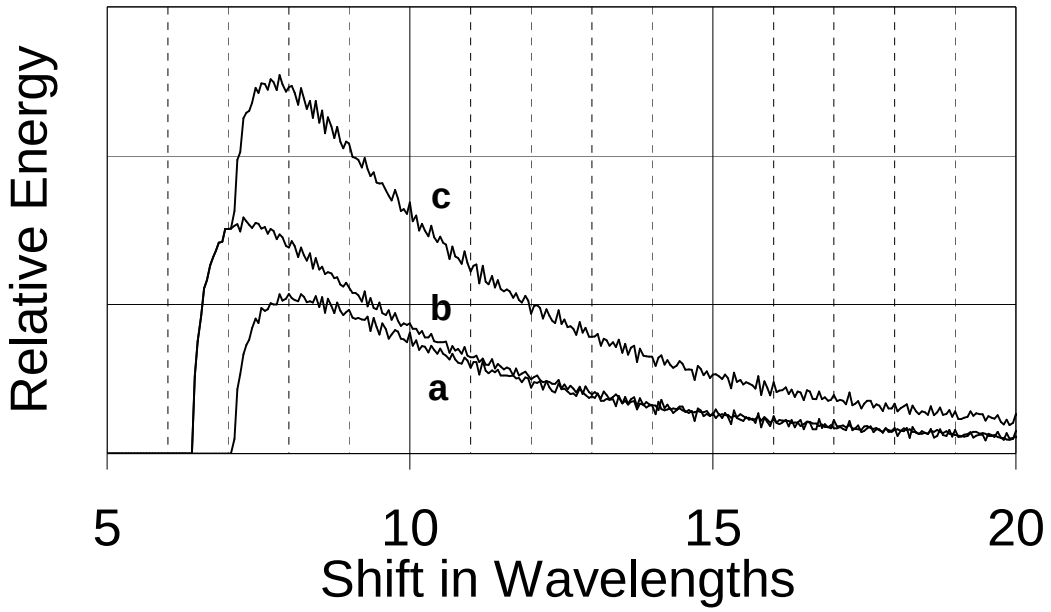


Figure 5 Goos-Hanchen Line Spread Function for two split components. Lines a, b, and c represent the trailing, the leading and the sum of leading and trailing components respectively. Divergence is .001 radians and delta angle ($\delta$) is .0001 radians.

The Effect of source divergence on Goos-Hanchen shift has been studied and numerically evaluated to predict the real world performance of observable sources. A line spread function has been found in graphical form, derived in analytical form, and reduced to a simplified closed form approximation. The model results support prior observations (finite shifts at critical angle[2, 4]) and should provide techniques for adequate interpretation of experimental shift measurements. The paper addresses to the possible sources of contradictions that may arise in the experimental observations. First, variations in beam quality, i.e. divergence, can produce differing results. Second, interpretation of beam shift is highly dependant on the measured beam shift features. Mean shift predicted by the equations is significantly different from edge shift observation. As

shown in Fig. 2-4, edge shift is nearly 60% of the mean shift. Maximum shift location depends on magnitude of divergence and which side of the critical angle that the incidence angle lays.

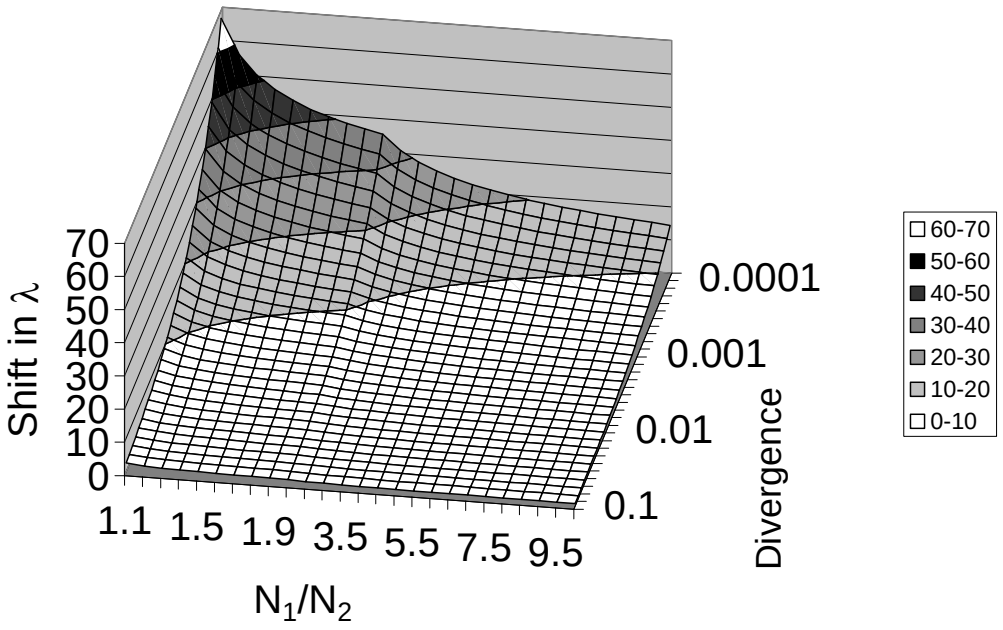


Figure 2-7 Mean Shift Sensitivities

If we combine the findings from equations 2-5, 2-6, and 2-9 and the graphical results seen in figures 4-6 it is possible to extend our observations towards practical applications of the Goos-Hanchen shift. Additionally a strong dependence of the shift on the ratio of refractive indices completes a design criterion for a potential white light imaging interferometer based on Goos-Hanchen shift.

Figure 2-7 shows that large shifts are obtainable by careful control the divergence angle. Note that the divergence is a limiting factor for observable shifts. Figure 2-7 also shows that the shifts can be amplified by reducing the ratio of refractive indices at the internal reflection boundary. The graph suggests that large single reflection shifts can be obtained by controlling these two

parameters. This method can also increase the reliability of devices that depend on the shift effect.

Furthermore, the functional form of the line-spread function appears to be well suited to interferometric purposes and may well lend itself to extensions of the phase shifting methods that have dramatically improved sensitivity of interferometry. Efficient design methods might be able to produce spatially distributed interferograms where localized variations in index of refraction appear as fringe line contours.

## *Measurement design considerations*

In traditional photographic experiments, a single shift value is extracted for a single rectilinear mask aperture. This method of single edge detection can be directly extended to simultaneous measurement of multiple adjacent edges when digital image capture and analysis is employed. Additionally, multiple adjacent apertures can then be added creating an array of sampling points. The individual apertures can be measured and analyzed independently to provide a means for measuring localized variations in refractive index or they can be combined for obtaining higher sensitivity to a nonlocalized mean refractive index. This allows for two measurements regimes to be performed over a sensing area rather than a single sensing line.

Prior method of implementing rectilinear masks require improvement and we suggest the use of stripped single mode optical fibers or the use of etched chrome-on-glass Ronchi rulings. The former possess very sharp edges but are difficult to position in uniform arrays. The latter can be fabricated in precise 2-dimensional arrays but possess diffraction limited edge roughness. Ronchi rulings are also suited for mounting onto piezo-electric positioning devices for positional stepping similar to the “jitter” camera used in super-resolution sampling[45].

In a design consideration for adjacent apertures, it must be noted that slit width and separation dimensions are affected by crosstalk. To minimize the crosstalk, Figure 5 can be used as a design guide for slit spacing and slit width. A recommended starting point would be to have both the slit width and slit spacing close to the mean shift shown in Figure 5. The limiting values of slit width could be comparable to edge shift and slit separation could be as much as twice the mean shift. Design trade-off must be considered relating to working source divergences, e.g., low source divergences will lead to higher slit width/spacing. This will reduce diffraction effects. However higher divergence will lead to $\lambda$ size shifts, which will increase diffraction effects. Thus slit widths of the order of wavelength will increase diffraction effects which are not desirable, however slit widths of the order 10 $\lambda$ will reduce diffraction effects and are desirable.

In addition, design trade-offs must be considered relating the working source divergence and desired sampling densities when the method is used for area coverage. Larger source divergences allow for denser sampling of an area but with a resultant reduction in overall sensitivity. Achieving higher sensitivity requires greater spread between sampling points in a gridded aperture configuration to account for the increases in lateral displacement near critical angle. Sources of one milliradian divergence for example will produce shifts nearly equivalent to single pixel widths of conventional ccd-imaging chips.

Multiple aperture methods are well suited for measuring distributions of refractive index variation over a sensing area. Ultra precise measurements of localized variations can be combined with distributed analysis methods for more accurate determination of mean refractive index.

## *Comparison of divergent method with Current research*

Researchers have reported attaining sensitivities of $10^{-6}$ index variation measurement[28]. For comparison purposes we can project the theoretical operating parameters for a divergent measurement system including source divergence, refractive index ratio, single vs multiple reflections, diffraction limited imaging, sub-pixel feature extraction, over sampling, and super-resolution.

First, the single reflection shift for a .001 radian beam is near $6\lambda$ at an operating refractive index ratio of 1.5. For a 1/3" CCD imager with a pixel size of 4 um and an optical magnification of 4:1, a single pixel size is on the order of magnitude of $2\lambda$ in the green. To detect a change of $10^{-4}$ in refractive index of the air would require resolving $D_{edge}$ to .15 pixels. This level of detection has been achieved. Details of sensitivity of refractive index derivation are given. To detect changes of $10^{-5}$ in n would similarly require .015 pixels discrimination which has also been attained with edge detection methods[46]. In a CCD array with the axis of the aperture aligned to the axis of the pixel through the imaging system, multiple parallel rows will see a stable sampling population allowing the use of 100 parallel sample rows in both the shifted and unshifted portions of the wavefront to provide the additional resolving power to attain $10^{-6}$ resolution on n.

Furthermore, sampling of parallel rows of apertures, improving the divergence of the source, and multiple reflections are all possible techniques to further extend the method.

### *Detectability limits of Divergent model*

The final theoretical task is to convert the new shift equations into a form where the sensitivity of imaging methods can be used to predict the sensitivity of an experimental apparatus to shifts resulting from changes in parameters such as refractive index. The development of sensitivity equations is rather straightforward from the previous equations,

$$D_{\perp edge} \equiv S = \frac{\lambda}{\pi} \frac{1}{\sqrt{2 * \cot(\theta_i)}} \frac{1}{\sqrt{\sin(\theta_d + |\delta|)}}. \qquad \text{(From 2-10)}$$

The sensitivity of shift to changes in refractive index can be found by the chain rule,

$$\frac{dS}{dn} = \frac{dS}{d\theta_c}\frac{d\theta_c}{dn} = \frac{dS}{d\delta}\frac{d\delta}{dn}. \qquad (2\text{-}26)$$

$\theta_i = \theta_c + \delta$ or $\delta = \theta_i - \theta_c$.

Using Snell's law, and taking the derivatives of both sides we obtain (2-27),

$\sin(\theta_c) = \frac{n_0}{n_1}$ Snell's Law

$$\cos(\theta_c) * d\theta_c = \frac{-n_0}{n_1^2} dn. \qquad (2\text{-}27)$$

If a change in δ results from a shift in refractive index the incidence angle remains constant we take the derivative of (2-10) with respect to δ,

$$\left.\frac{dS}{d\delta}\right|_{\theta_i=const} = \frac{-\lambda}{\pi}\frac{1}{\sqrt{2\cot(\theta_i)}}\frac{\cos(\theta_d+|\delta|)}{\sqrt{\sin^3(\theta_d+|\delta|)}} \quad . \tag{2-28}$$

For $\theta_d + \delta < .01$ we can approximate the expression to,

$$\left.\frac{dS}{d\delta}\right|_{\theta_i=const} \cong \frac{-\lambda}{\pi}\frac{1}{\sqrt{2\cot(\theta_i)}}\frac{1}{\sqrt{(\theta_d+|\delta|)^3}} \tag{2-29}$$

$$\left.\frac{dS}{dn}\right|_{\theta_i=const} \cong \frac{\lambda}{\pi}\frac{1}{\sqrt{2\cot(\theta_i)}}\frac{1}{\sqrt{(\theta_d+|\delta|)^3}}\frac{n_0}{\cos(\theta_c)n_1^2} \quad . \tag{2-30}$$

For practical estimation, consider a fused silica to air interface at critical angle,

$n_1 \cong 1.4,\ \theta_c \cong \frac{\pi}{4},\ and\ \delta = 0$

$\left.\frac{dS}{dn}\right|_{\theta_i=\theta_c^+} \cong \frac{\lambda}{\pi}\theta_d^{-3/2}$ (Fused silica approximation).

If we define the detectability threshold for shift measurement as $T_s$ and the detectability threshold for refractive index variation as $T_n$ then,

$T_n = \frac{T_s}{dS/dn}$, roughly proportional to $\theta_d^{3/2}$, i.e. a 10-fold improvement in divergent angle yields more than a 30-fold improvement in shift detection.

To detect a change of $10^{-5}$ in refractive index of the air for $\theta_d$ = 0.001, would require resolving $D_{edge}$ to .015 pixels, i.e. $T_s$ = 0.1 λ which is common practice today.

### *Divergence Model Conclusions*

1. The divergence model is compatible with prior results from Gaussian beam analysis.
2. Source divergence for planes waves is similar, but not identical to beam waist parameter for Gaussian beam.
3. Introduction of beam divergence leads to a simplified expression for spatial dispersion.
4. Divergence is the primary limiting parameter for enhancing shift magnitudes.
5. A new measurement parameter based upon edge shift behavior has been defined and is shown to be well behaved and highly sensitive to angular shift and refractive index variation. The edge parameter shows monotonic behavior on either side of critical angle, is independent of spot splitting, and has a monotonic slope which is discontinuous at critical angle.
6. Current technological capabilities exist to support precise imaging and edge localization.

# 3. Goos Hanchen Divergence Model - Practical measurement considerations[51]

## *Introduction*

In chapter 2, we presented and discussed a novel method for mathematically modeling the distributed Goos-Hanchen[3, 47] shift function in the presence of a finite divergence white light source incident near critical angle for total internal reflection. Here we will follow-up on additional general observations and further generalized closed form equations. We extend our prior discussion of quantitative methods for interpreting Goos-Hanchen.

The purpose of the prior work was to establish a mathematical formulation for describing the effects of source divergence on the Goos-Hanchen shift for nonideal planes waves. The dependence of shift functions on parameters including source divergence, refractive index ratios, and alignment angle was investigated. In this letter we build on that foundation and address the sensitivity and detectability needs for using the divergence model to conduct and interpret a new class of Goos-Hanchen shift experiments with real sources. Two distinct regions of operation are identified: alignment angle, $\delta$ less than divergence angle, suitable for static measurements e.g. source collimation; and $\delta$ greater than divergence angle, suitable for dynamic measurements e.g. variation of refractive index in rarer medium.

We first address the sensitivity of mean beam shift for the different cases of $\delta$ being less than or greater than divergence. When $\delta$ is less than the divergence angle, the observed shift is nearly independent of angular alignment. When $\delta$ is greater than the divergence angle, the shift becomes highly dependant on $\delta$. It is worth noting that variations in index of refraction cause

variations in critical angle, which are mathematically equivalent to shifts in $\delta$, and hence have similar shift sensitivities when operating above the divergence angle.

Next we will discuss the effects of finite apertures on the observable shifts. While the Greens function for point shifts are given, the detectable signals consist of aperture convolutions. Below divergence, the semi-infinite nature of the shift function necessitates use of a step aperture. Above divergence, the bounded nature of the shift function allows for finite width apertures or rectilinear mask apertures. In both cases we must define feature detection in terms of an edge shift function.

Finally, we will discuss the relevance of image processing techniques for precision measurements and the potential for using active super-resolution edge detection methods. Such techniques have strong potential for extending the detectability threshold for changes in refractive index in the rarer media.

## *Approach*

We know from the prior mean shift results and the paraxial analysis of Puri and Birman[17] that observable mean shifts are nearly independent of alignment within roughly half of the divergence angle of the source. In this narrow range of angular operation the observable shift is virtually independent of incidence angle contrary to the straightforward Goos-Hanchen shift equation. The region of near constant shift is a physical limitation of using nonideal light sources and not a contradiction of the theory. This region is predicted for plane waves as a function of divergence and for Gaussian beams as a function of minimum beam waist that is proportional to divergence.

We also know that mean shift reaches a peak value at some distance from the critical angle. This makes mean shift a poor technique for precisely locating critical angle. We would rather seek to find a measurable quantity which reaches peak value precisely at critical angle and is symmetrical about the critical angle. We also seek a monotonic behavior in both function and slope.

To these ends, we consider the edge shift function. Given a source divergence and an angle of incidence we can mathematically express the minimum shift seen by components of the incident plane wave which have the greatest deviation from critical angle. These components set a floor value for the shift which a step aperture shadow will see at internal reflection.

First we numerically evaluate the mean shift function at critical angle to verify our model. Figure 1 shows numerical model plots of mean shift at critical angle as a function of source divergence for three ratios of refractive index.

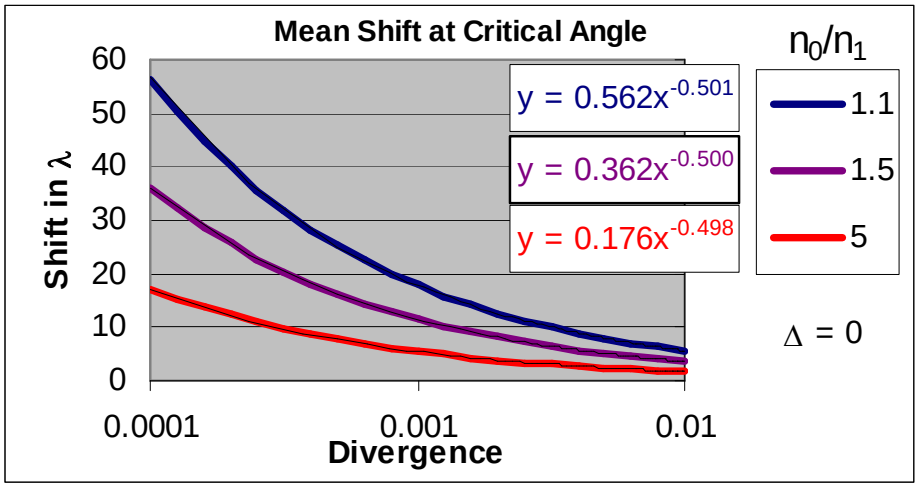


Figure 3-1 – Mean Shift at Critical Angle

For the divergence model we are using here, the shift functions in Figure 3-1 show a mathematical relationship of

$$Shift \propto \frac{1}{\sqrt{2*\cot(\theta_i)}\sqrt{\theta_d}}, \text{ at critical angle.} \tag{3-1}$$

This derives from the classical equations[6, 7].

$Shift \propto \frac{1}{\sqrt{\delta}}$ and the approximation $\sin(\theta_d) \cong \theta_d$,

where $\theta_d$ is the source divergence angle and $\delta$ is the angular error. Equation (3-1) works at critical angle when δ is zero and is related to the minimum edge shift function,

$$Shift_{\min} \propto \frac{1}{\sqrt{\delta + \theta_d}}. \tag{2-10}$$

The effect of source divergence stems from the interaction between the alignment angle and the divergence angle. As δ increases above $\theta_d$ the alignment terms becomes dominant. As δ approaches zero the divergence term becomes the limiting factor in the observable shift. The minimum shift seen by components of a divergent wavefront becomes a bounded proportionality and the limiting observable shift at critical angle becomes equation (3-1). Our divergence model verifies our earlier prediction that the minimum edge shift cast by a step or slit aperture can be shown to be the classical shift equation evaluated at the sum of the alignment angle and the divergence angle.

The classical mean shift functions have been shown to be cumbersome and asymmetrical about the critical angle in both theory and in experiments. In contrast the edge shift function is symmetrical as can be seen in figure 3-2. Additionally the slope of the edge shift function is antisymmetrical and discontinuous at critical angle.

Thus the edge shift at critical angle can be used for precise measurement of critical angle and source collimation. This regime is relatively insensitivity to errors in alignment which are less

than half the divergence angle due to the dominance of the divergence term. This method is also suitable for measuring mean shift variations resulting from changes in alignment of the source.

For alignment applications the sensitivity of the observable mean shift is proportional to the slope of the shift function. For incidence angles above divergence, the δ term becomes dominant. For incidence angles below divergence angle the divergence angle becomes dominant. Maximum slope is slowly approached as δ goes to zero. The sensitivity formula reflects the dependence of shift on alignment angle in the region above the divergence angle.

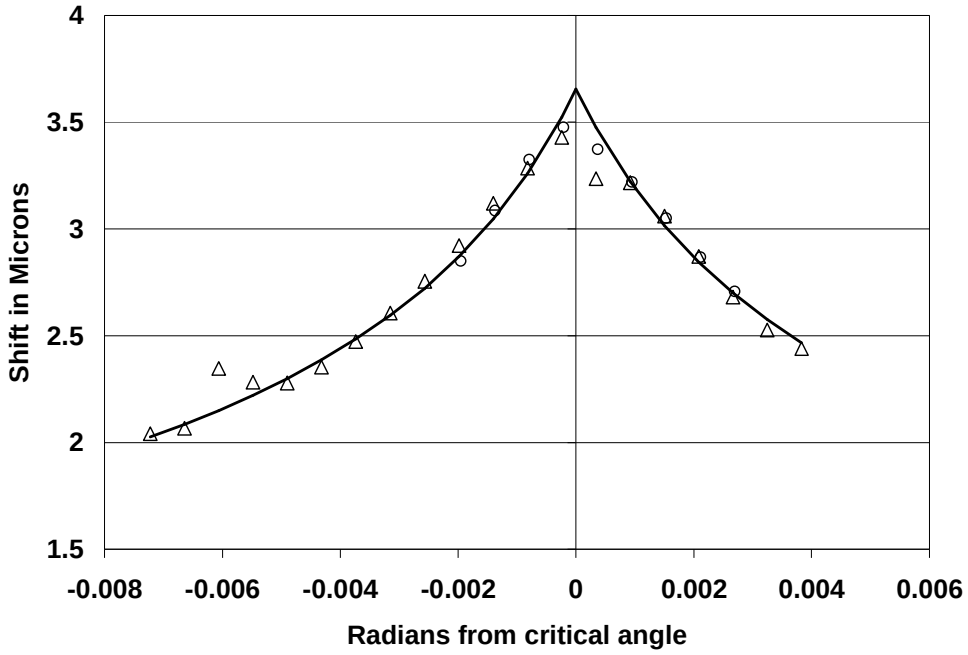


Figure 3-2 – Edge shift and slope vs. δ (radians)

$$dS \propto -\frac{1}{\sqrt{2*\cot(\theta_i)}\sqrt{(\theta_d+\delta)^3}}d\theta \text{ In } \lambda \text{ per radian} \qquad (3\text{- }2)$$

It is easily seen that high sensitivities to changes in alignment angle can be obtained with lower source divergence when operating with $\delta$ near the critical angle and at low ratios of refractive index. Additionally, changes in refractive index alter the critical angle, effectively shifting the alignment angle for a static apparatus. This provides a powerful technique for

measuring differential change in refractive index of the rarer media by operating the measurement apparatus slightly above the critical angle of the source.

### *Green's function in the region* $\delta < \theta_d$

In the operating region near critical angle a closed form Green's function exists to describe the spatial dispersion. This function has two components which correspond to the relative intensities of the wave components above and below critical angle. We recast the Green's function (2-24) for the leading spot and later recombine the trailing edge spot.

$$I_{LSF} = \frac{I_0}{\lambda\theta_d}\sqrt{2\cot(\theta_i)}\sqrt{(\sin(\theta_d+\delta))^3}\left(\frac{D_{edge}}{x}\right)^{b_L/2}\sqrt{\left(\frac{D_{edge}}{x}\right)^{a_L-b_L}-1} \qquad (3\text{-}3)$$

The combined form is valid when the critical angle lies within the cone of divergence of the source. As $\delta$ increases from 0 to the divergence angle, the amount of total light flux increases in the leading portion of the cone and decreases in the trailing portion of the cone. Simultaneously, the minimum shift of the leading edge decreases and the minimum shift of the trailing edge increases. These are the $D_{edge}$ terms in the Greens function. Essentially spot patterns are created, intensity in the near spot sees less shift with higher total flux while intensity in the far spot sees a larger shift with a diminishing total flux. As the delta angle increases the far spot becomes increasingly less significant to the total energy shift. This model also provides an alternative explanation to the weak trailing spots observed is earlier experiments[9]. Previously they were explained as diffraction effects.

It is straightforward to show that the peak intensity shift for each of the spots occurs at,

$$D_{peak} = D_{edge}\sqrt[(b-a)]{\frac{b}{a}}\,. \qquad (3\text{-}4)$$

For values of a and b between 6 and 10, $D_{peak}$ is within two percent of 1.14 * $D_{edge}$. This valuable equation allows us to make an accurate direct calculation of the peak intensity shift position given only the divergence and angle of incidence of the plane-wave. The importance will be seen when we consider the effects of aperture on imaging systems.

The power coefficients are equations (3-3) and (3-4) are not constant in general. They vary with the divergence angle and $\delta$.

### *Working Apertures*

Proper choice of aperture type plays a strong role in system performance and depends on the region of operation of the measuring system. Below divergence the impulse response is semi-infinite and is best suited for use with a step aperture or a single side of a rectilinear mask. Above divergence where the impulse response has finite dispersion, the use of slit apertures is indicated.

For the former case we convolve the combined spot shifts with a step function and truncate the end portion, we can simulate the intensity distributions that an observing system will see for a semi-infinite or step aperture.

This can be seen in figure 3-3 where the overlap of the spots is no longer visually apparent. Variations in the slope of the curve can be extracted with careful image processing techniques. For the leading and trailing components, a local extrema in slope values exists at a shift of ~1.14 $D_{edge}$. The peak value of the slope of the convolution corresponds to the peak intensity of the line spread Green's function as predicted by the convolution theorem and the fundamental law of calculus.

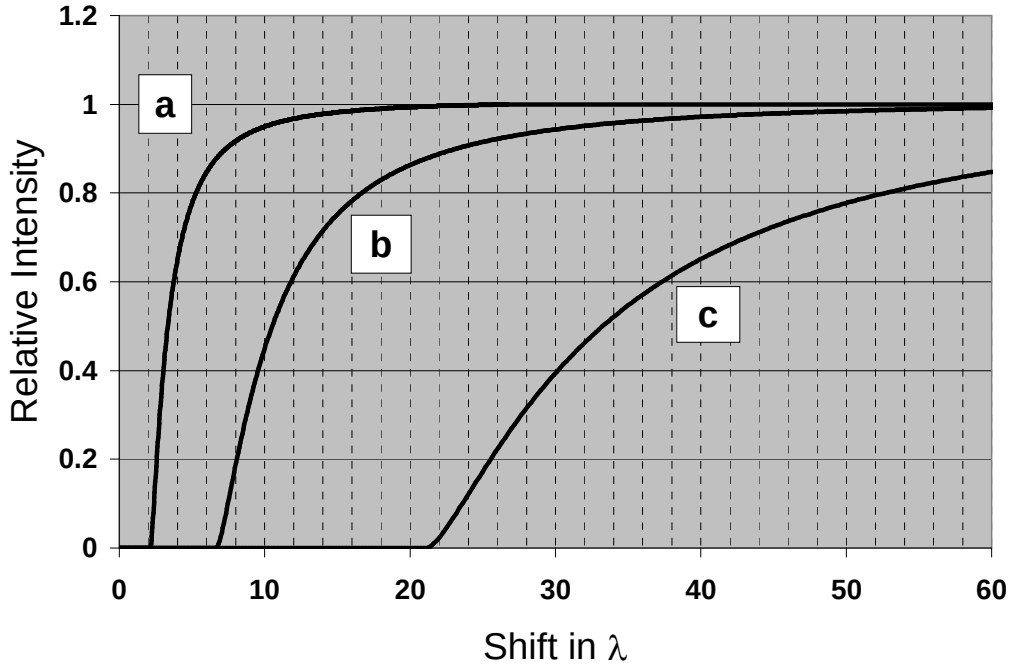


Figure 3-3 Intensity distributions of step function convolutions of impulse response – for divergences of a-0.01, b-0.001, and c-0.0001

A step function convolution of the Green's function produces a readable intensity transfer function whish appears well suited for traditional sup-pixel imaging methods. The suitability is related to the absence of high frequency components in the slope variations of figure 3-3. If precise locations of inflection points are required image sub-sampling methods can be employed.

### *Green's function in the region* $\delta > \theta_d$

In the region above the divergence angle a closed form equation for the Green's function is available from chapter 2, equation (2-23) (with simplifications). A full expansion is also available in chapter 2.

$I(D_\perp) = \frac{2I_0}{\lambda\theta_d^2}\sqrt{\theta_d^2 - d^2}\sqrt{2\cot(\theta_i)}\sqrt{(\delta - d)^3}$ , where d varies continuously from - $\theta_d$ to $\theta_d$ . Additionally,

$$d = \delta - \lambda^2 / \pi^2 D_\perp^2 2\cot(\theta_i).$$

Numerical generation of the evolution of shape of the output pulse produces several useful observations. First, the shape depends on the ratio of $\delta / \theta_d$ . Not surprisingly, the ratio of peak shift to edge shift decreases asymptotically to 1 and mean shift converges rapidly to peak shift as the pulse becomes nearly symmetrical. The shift pulse is now completely bounded permitting use of properly spaced slit apertures to enable array sampling without crosstalk. The bounded property also permits meaningful interpretation and measurement of the mean shift values (see figure (3-4).

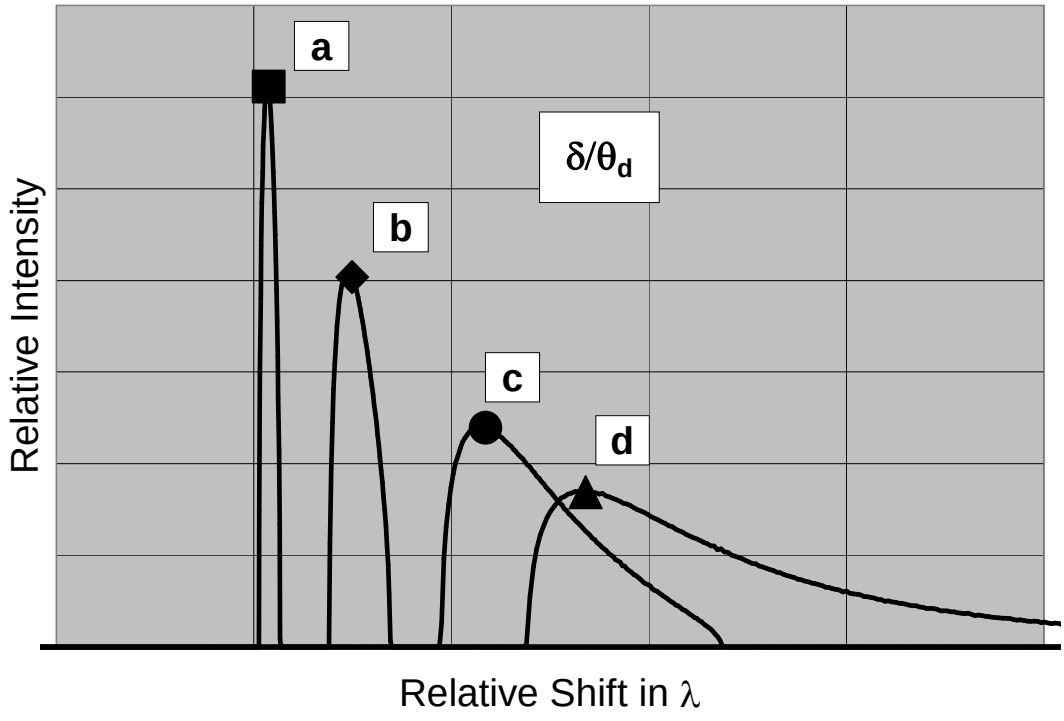


Figure 3-4 - Impulse response shape evolution. Pulse shapes are shown for ratios of alignment angle to divergence angle from 1 to 10, a-10, b-5, c-2, and d-1

For our model we select an aperture which is approximately twice as wide as the peak shift at 1.5 * divergence. This width completely encapsulates the bounded pulses for delta angles above 1.5*divergence. The shape of the resulting shaped pulses is shown in figure 3-5. The leading and trailing edges of the convolution contain precise information about the locations of Dedge and Dpeak. Extraction of this information can be achieved by sensitive image processing techniques when used with accurate numerical models. Near the beginning of the leading edge the rise profile of the pulse should be very nearly parabolic according to our current models.

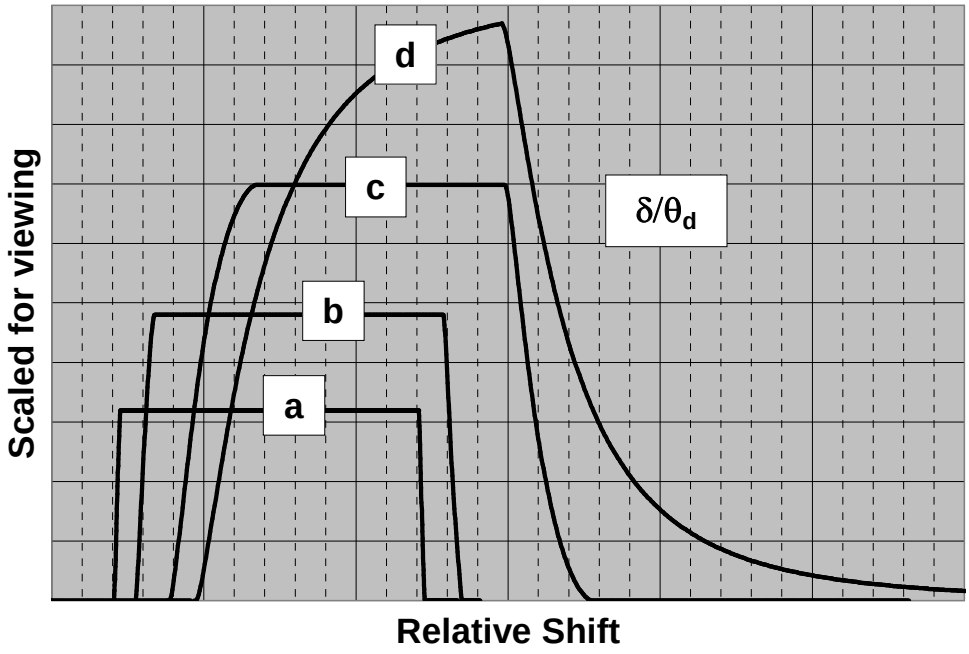


Figure 3-5 Slit Convolution shapes for various ratios of delta to divergence angle from 1 to 10, a-10, b-5, c-2, and d-1

## *Experimental design considerations*

We now address three phases of experimental considerations: experimental setup, alignment and calibration, and special imaging requirements

*Experimental setup*

Quantitative experimental verification of the single reflection Goos-Hanchen shift can be performed by placing a rotational prism between a divergent source and an image acquisition and analysis system (see figure 3-6). Using either a thin slit, a wide slit, a rectilinear mask, or a semi-infinite slit the windowed, reflected, and shifted plane wave can be read on an image sensor. As the prism is rotated towards the critical angle, the shift can be recorded and plotted against the angular encoder position of the goniometer.

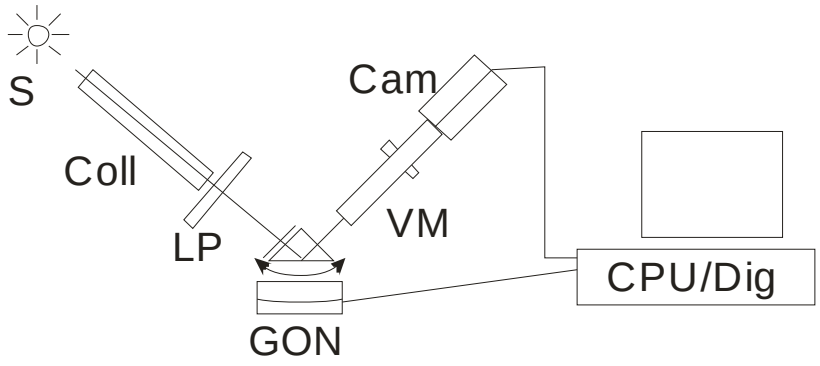


Figure 3-6 Experimental setup: Cam-camera; VM-video microscope: Gon-goniometer; LP linear polarizer; Coll- collimator; S- Source; Dig-digitizer; CPU-processor

By simultaneously recording and analyzing the shifted image, the critical angle, maximum shift, and slope variations can be extracted.

*Alignment/Calibration*

Sweeping from well above critical to well below critical angle reveals the divergence limited critical angle shift. At the critical angle the slope of the edge shift function reverses sign allowing for interpolation schemes to resolve the true location of the critical angle and the

maximum attainable edge shift. The slope functions themselves contain information which can be used to evaluate the divergence.

If access to the beam path is available in the rarer media, then initial alignment can be set by the disappearance of the transmitted wave in the rarer media. A rough measurement of the shift at this point can provide a working scan range for the rotation stage.

*Special imaging requirements*

Prior experimental designs have sought to amplify the shift by multiple reflections[2]. The first experimental tests utilized photographic recording which was later replaced by beam intensity profiling[12]. Following the work of Canny[32] and others such as Bao, Zhang, and Wu[48] image processing and precision edge detection provide a new approach for enhanced shift measurement methods. These can increase the resolvability by applying image processing methods with the sub-pixel enhancements and by applying video microscopes with image magnification. These combined methods now provide a method of detecting and localizing edge and slope features of the convolved outputs rather than mean positions of skewed spots.

For Goos-Hanchen edge shifts the feature of interest becomes the position of maximum slope of the aperture convolution which we have shown to be located at the peak position of the impulse response function. The existence of a numerical relationship between $D_{peak}$ and $D_{edge}$ allows us to directly convert measurements of $D_{peak}$ into estimators of $D_{edge}$ which can validate the classical equations for shift dependence on incidence angle. In practice, best results are obtained when the edge is slightly defocused and the lateral edge profile is nearly normal to the sensing direction of the digital filter.

Figures 3-4 and 3-5 show the convolution of the Green's function with a step and slit aperture. The shift and smear of the aperture edge in the reflected wave is seen for three values of

divergence. At very low divergences (.0001 radians), an unaided 1:1 imaging system could clearly distinguish the shift to fractions of a pixel (approximately 10λ). As the divergence increases to .001 radians some magnification would be required but the effect is still within the diffraction limit.

At higher source divergences, .01 and greater, the diffraction limit on the imaging system requires a more sophisticated approach. Super-resolution techniques combined with suitable sub-pixel algorithms will provide the necessary extension to measure shifts below the diffraction limit of the optical system. Additional sampling densities can be obtained by mounting the image sensor chip on a piezo-electric nanopositioner capable of locating the chip to a suitable fraction of a pixel position[46].

### *Summary*

In this paper we have presented the quantitative treatment for a new class of experiments which exploit the natural source divergence characteristics of the Goos-Hanchen shift. These methods are ideally suited for use with modern image processing techniques creating a class of measurements whose sensitivity depends on the divergence characteristics of the source: 1) We see that maximum sensitivity to change in alignment or refractive index at critical angle; 2) The symmetry of edge shift sensitivity about the critical angle is a valuable tool for precisely locating critical angle and quantitatively determining the source collimation; 3) The divergence method is applicable for a variety of aperture types depending upon region of operation. Bounded responses which occur when operating above divergence angle can utilize arrays of parallel slit apertures for increasing sampling density while unbounded responses (δ below divergence) require step or rectilinear mask apertures; 4) Increasing the source divergence leads to a

reduction in the observable shift which requires a higher sampling density to produce equivalent results. The availability of imaging and image processing methods, including optical magnification, sub-pixel edge detection, and oversampling, satisfy this need for extending the measurement accuracy for larger source divergences. A combination of the multiple methods described can provide a potential powerful tool for high precision measurements of variations of refractive index, or for discrete sampling of variation over an area of interest.

# 4 -Image Processing Considerations[50]

## *Introduction*

This effort was undertaken to support research thrusts into the exploitation of the Goos-Hanchen shift which occurs at internal reflection interfaces. The shadow of a step aperture shifts longitudinally at an internal reflection interface. The shift increases as the angle of incidence approaches the critical angle due to the presence of an evanescent wave in the rarer media. In the ideal case, the shift becomes infinite but in all measured real cases the shift magnitude is controlled by the divergence of the incoming wave and reaches a maximum at the divergence angle. Attempts to exploit the effect for physical measurement devices have been made using Gaussian beam and spot position detection systems. We seek to mirror the studies of Gaussian beams with parallel studies of the G-H effect on divergent planes waves. By switching from mean spot position monitoring to shadow edge detection we create a path for using plane waves to perform high precision monitoring. To make the system work requires advances in sub-pixel edge detection combined with statistical sampling regimes. Ultimately, a resolving power of .001 pixels combined with a .001 milliradian divergent source can lead to a measurement system capable of detecting changes in refractive index smaller than the order of $10^{-6}$ in n. Resolving power is directly proportional to the sub-pixel image processing performance and proportional to the 1.5 power of improvements in source collimation of the plane wave. The methods and

techniques have direct transferability to the problems of precise measurement of rigid body motion, thermal expansion monitoring, target alignment, and a host of other applications.

The purpose of this paper is to describe the development of image processing methods required to support a high precision differential position locating system. The positional objects are research grade edges of chrome etched on glass. Such objects are typical in glass slides of USAF (United States Air Force) standard resolution targets and Ronchi rulings which can be readily obtained through commercial sources. Encapsulated in the localization process is measurement and analysis of edge straightness and roughness which plays a limiting factor in the resolving power of the system as a whole.

Modern image processing methods have greatly expanded the opportunities for engineering innovation. Using filter techniques developed in the 60's and 70's combined with straightforward numerical processing techniques it is now possible to measure feature edges with resolutions approaching and beyond .001 pixels. Such resolutions have been attained by combining difference of Gaussian Canny[32] filters with oversampling and careful tuning of parameters. Additional techniques for increasing sampling density may result in future improvements of resolution and sensitivity

In this regime we encounter resolving limitations which come from the target edges themselves. Edge roughness and quality of targets become critical factors in pushing back the edge of the envelope. Several different edge materials have been tested and differing choices are

available for different applications. Additionally, mount stability and motion direction become correlated factors in limiting resolving power.

## *Method*

Preliminary experiments designed to support practical application devices have been performed using a ccd-imager combined with a video microscope. Our experiments use an Edmund Optick EO-3BW 1/3" CCD imager with an Edmund Optick VZM-1000 2.5x-10x zoom video microscope. Data is captured on a Matrox Meteor II 8-bit digitizer. These components were selected for their moderate cost and performance characteristics. The target object is etched chrome on glass USAF STD resolution target with features as small as 228 lps/mm. The camera is mounted vertically above the slide and a diffusion screen is placed 2 inches below the target. Backlit illumination is from the diffuse surface on the backside of the target.

First we seek to characterize the edge straightness, roughness, and angular alignment to our imaging system. The ion beam lithography used in making Ronchi gratings has a beam spot of .3 microns. The manufacturer specifies the ruling edges to be within 1 micron of nominal position. We measure the edge positions using a Canny[32] type edge detection scheme.

Many approaches for edge detection have been studied by various authors. The most common methods remains the derivative filters of various types and enhancements. The theory behind these methods goes back to the work of Canny who initially established three criteria for judging suitability of edge filters. The three criteria are: good detection; good localization, and low response multiplicity. In our experimental setup detection is near perfect and multiple responses

are virtually nonexistent. This is a direct result of using clean precision targets and low noise imaging systems. As a result high contrast edges are obtained and the localization criteria for performance become our primary interest.

Demigny[34] has shown that the optimum localization occurs when the filter coefficients decrease from center towards zero at the filter edges. Shen's[34] one dimensional IIR filter which we use as a starting point for our studies can be derived from Canny's theory under circumstances such as ours where the probability of multiple responses can be reduced to zero, i.e, a single edge with sufficient contrast to overpower any noise present in the plateau regions of the image. For imaging of high contrast etched chrome on glass this condition can be easily met with sufficient illumination intensity and appropriate control of stray light.

This results in the form of an FIR filter which can be simply described by

$$F[n] = \sum_{i=-k}^{k} \frac{x[n+k]e^{-\alpha k}}{f(i)}, \quad i \neq 0 \qquad \text{The magnitude of f (i) increases with } |i| \qquad (4\text{-}1)$$

Subpixel locations are then found by fitting a quadratic polynomial to the highest output points in the filtered image and the two surrounding points. This results in a very straightforward calculation of the sub-pixel value. What then remains is the empirical work of establishing the values of a, f (i), and k.

Preliminary results from the edge profiling revealed the surface roughness of the edge to be much larger than the resolution of the edge filter. This roughness makes it impossible to determine the true position of the edge for theoretical purposes. Hence, the absolute accuracy of

any individual measurement cannot be found. We can however compare the relative performance of different filters by comparison of relative noise levels using a second derivative approach

Filter tuning is done by a Laplacian noise comparison. A 3 point rolling average is compared to local values to establish a noise figure. This is equivalent mathematically to a Laplacian filter applied at the point as can be seen form equations (4-2) and (4-3). The figure is not a meaningful measure of sensitivity or accuracy but is valuable for comparison of Laplacian noise levels. The Laplacian noise levels are useful to measure local random variation of individual points in the dataset. This is particularly necessary when the true roughness of the target is larger than the resolving power of the sub-pixel algorithms. Mathematically this function is the second difference equation for the dataset.

$$L_{noise}[n] = \left( \frac{x[n-1] + x[n] + x[n+1]}{3} \right) - x[n] \tag{4-2}$$

$$L_{noise}[n] = \frac{x[n-1]}{3} - \frac{2x[n]}{3} + \frac{x[n+1]}{3} \tag{4-3}$$

The second difference equation is also a ceiling value for the measured edge roughness since it is directly affected by both the edge roughness and the uncertainty of the edge detection process itself.

The most telling test of a sub-pixel algorithm is how well is can measure uniform motion or in the static case how stable individual measurements are for a rigid body. Factors such as

mechanical vibration, thermal variation, and electronic noise all affect a static test. Electronic noise and low frequency mechanical vibration can be integrated out by summing sequential frames. Thermal variations are much slower and standard shop practice is to allow the test article to soak in the test room environment for a suitable period of time. For chrome on glass slides 10-15 minutes under constant illumination is usually suitable.

The accuracy of rigid body tracking is enhanced by summing multiple edge points into a common measure of relative edge position. If this data was uncorrelated we would expect accuracy to be improved by the square root of the number of samples. In practice adjacent pixels correlate by lateral vibration of the test article and typical error improvement using spatial averaging result is improvement more on the order of the cube root of the number of samples.

An alternate approach in theory is to misalign the edge of the target very slightly relative to the axis of the imager and intersperse the separate lines across the edge into a single super-resolution cross sample of the average edge profile. In theory this is straightforward but in practice the edge roughness of the target drives a requirement to sort the individual lines into a monotonic set of weighted edge locations. This method will ultimately lead us to a study of edge detection enhancement by scale multiplication as outlined by Bao, Zhang, and Wu[48].

Finally, we must evaluate which metric provides the most precise responses based upon the specific intended application. In our deployment activities we will focus on the relative longitudinal motion of near parallel line segments. If no torque of the target is expected we can either construct a least squares line fit and measure the offset at the interface or we can measure

the difference between the mean positions of the individual line segments. The mean positions method is highly sensitive to target rotation while the line intersection method is highly sensitive to lateral shifting of the target. Which is better is most often determined by physical setup of a particular experiment.

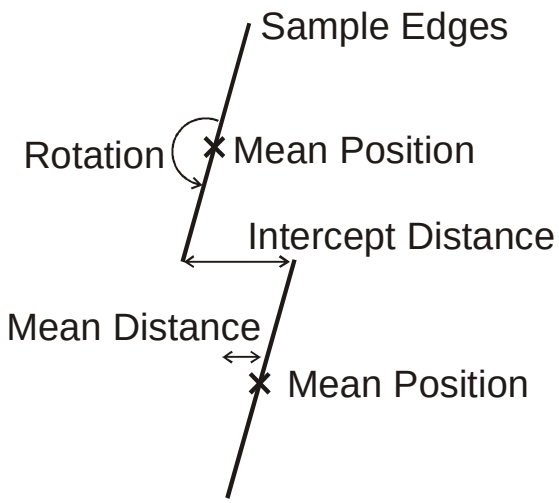


Figure 4-1 Geometrical line sensing arrangement

Figure 4-1 shows the geometrical setup for our line locating algorithms. Two adjacent line segments are sampled and located separately. The mean position of each segment is calculated from the discrete point data as are the slopes and midline intercept positions.

Intercept distance is sensitive to independent rotation of either segment. Slopes and intercepts are also sensitive to the effects of line roughness under conditions of vertical displacement or vibration.

Mean distance is sensitive to rigid body rotation resulting in cosine errors on the measured direction. For these reasons, calculations are made for each component of motion, twist, and rigid body rotation.

## *Results*

Our initial testing is to establish the resolving power of the video microscope. Figure 4-2a is a USAF STD resolution target at minimum zoom. All components of the target are seen with blurring seen along group 7. A close up of a section of group 0 element 4 at a line density of ~1.26 cycles per millimeter is used for testing. The target has been aligned to a slope of .001 pixels per pixel or 1 milliradian.

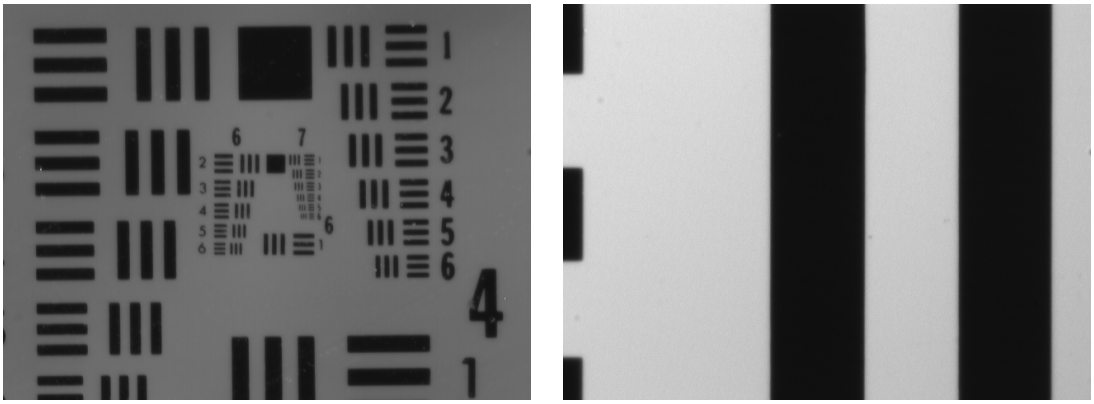


Figure 4-2 – a) USAF STD Res Target b) Close-up of Group 0 Element 4

Figure 4-2a is a wide angle shot of the USAF STD resolution target taken with a standard 30mm lens. Figure 4-2b shows the video microscope performance at a minimum zoom of 2.5x.

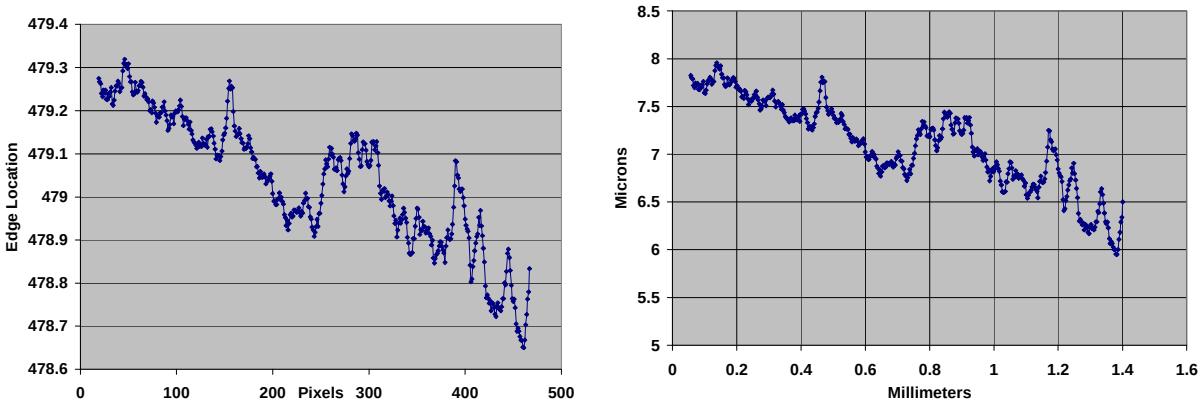


Figure 4-3 - a) Target Edge Profile b) Profile in microns

Figure 4-3 a) and b) shows a typical section of a vertical edge. The Y-axis of the graph represents the horizontal position of the edge detection. The X-axis represents the vertical position of the sample from the top of the image. We note a slight tilt of the edge relative to vertical, roughness on the order of .2 pixels and a step offset in the edge around the 250 pixel position. All of these are typical observations for an etched edge on glass. Pixel size is known from measurement to be approximately 3-microns and .2 pixels are approximately .6 microns.

We see from figures 4-3a and 4-3b that the segment under evaluation has surface roughness on the order of .5 um and a step shift of about .5 um. Both values are consistent with the manufacturer's specifications for the slide. Both graphs clearly demonstrate the image processing ability to detect the surface roughness of the target.

Next we turn our attention to determining an optimum width for the filter kernel. Wider kernels produce better results in general but they do so at the expense of processing cycles. To

optimize throughput we seek to find the minimum width of the kernel which provides near optimum error. Figure 4-4a shows the Laplacian noise performance for three different forms of denominator function in equation (4-1): diamonds represent a constant denominator; circles represent a linear increase in the denominator from the center of the kernel; and triangles represent a quadratic increase in the denominator. Kernel widths are tested from 3 pixels to 19 pixels. Figure 4-4b shows the intensity variations across a typical edge position in a transition from bright to dark.

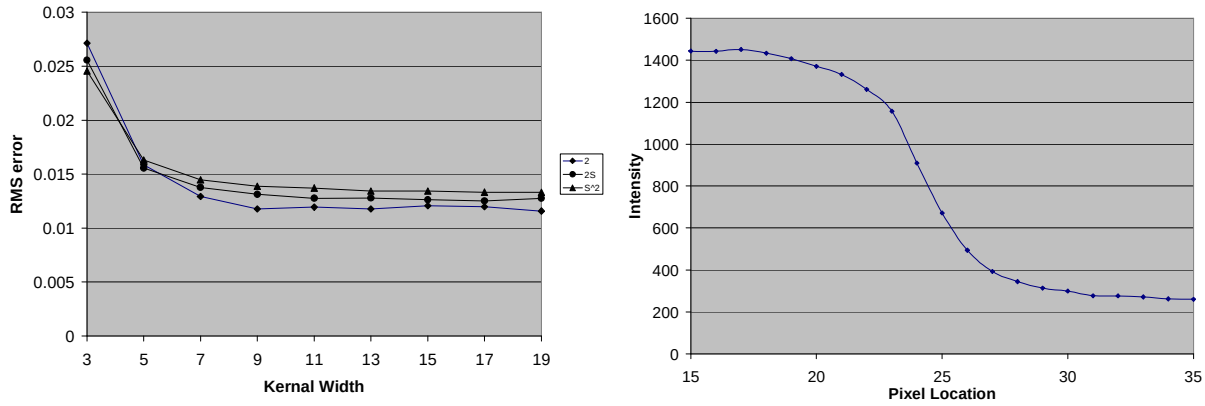


Figure 4-4 – a) Laplacian error as a function of kernel size b) - Gaussian edge blur

In the Gaussian edge blur graph we see the active edge transitions region to be approximately 9 pixels. This width corresponds to the point of diminishing returns in the Laplacian error function. Increasing the kernel size beyond the width of the transition zone produces no meaningful improvement in filter performance at the expense of an increased processing load. It should be noted that increasing the magnification of the video microscope will increase the blur width and necessitate adjustment of kernel width. This is because the imaging system a 2.5X is

operating on the edge of the transition zone into the diffraction limited region of magnification. At 2.5x magnification the ccd-sensor has an image field pixel size of nearly 3 microns. At 10x, the limit of optical magnification for our video microscope, the pixel size falls below 1 micron and diffraction effects begin to become apparent.

| Kernal Size | Filter Denominator | | |
|---|---|---|---|
| | 2 | 2*i | i^2 |
| 3 | 0.027147 | 0.025569 | 0.024559 |
| 5 | 0.015872 | 0.015564 | 0.016319 |
| 7 | 0.012921 | 0.013778 | 0.014468 |
| 9 | 0.011777 | 0.013123 | 0.013881 |
| 11 | 0.011945 | 0.012758 | 0.013717 |
| 13 | 0.011771 | 0.012772 | 0.013424 |
| 15 | 0.012082 | 0.012629 | 0.013428 |
| 17 | 0.011969 | 0.012522 | 0.013334 |
| 19 | 0.011573 | 0.012771 | 0.013313 |

Table 4-1 Laplacian noise of edge

Table 4-1 gives the numerical values for figure 4-4a. Variation with kernel size is dramatic below the blur width. Variation with denominator function is seen to be less significant. Curiously, these results suggest that a constant value in the denominator produces a slightly better result than an increasing value function as has been previously claimed. This may be a special case for a target with well controlled noise. Minimum Laplacian noise levels are seen to be near .012 pixels for the constant denominator kernel with widths of 9 and larger.

To estimate the resolution of an individual edge measurement we must evaluate the noise floor of the experimental setup. We do this by taking multiple measurements along a vertical edge and repeating the process at multiple times. Figure 4-5 show a surface plot of 40 points

measured at 40 consecutive time positions. The resulting rough surface is representative of the process variation which limits the repeatability of the measurement method. The RMS roughness for the sample shown in figure 7 is .014 pixels. The plot in figure 4-5 has been adjusted for rigid body drift over the duration of the experiment. Horizontal features which are barely discernable in figure 4-5 are electronic noise in the imager and digitizer which affect all measurements from their respective time samples.

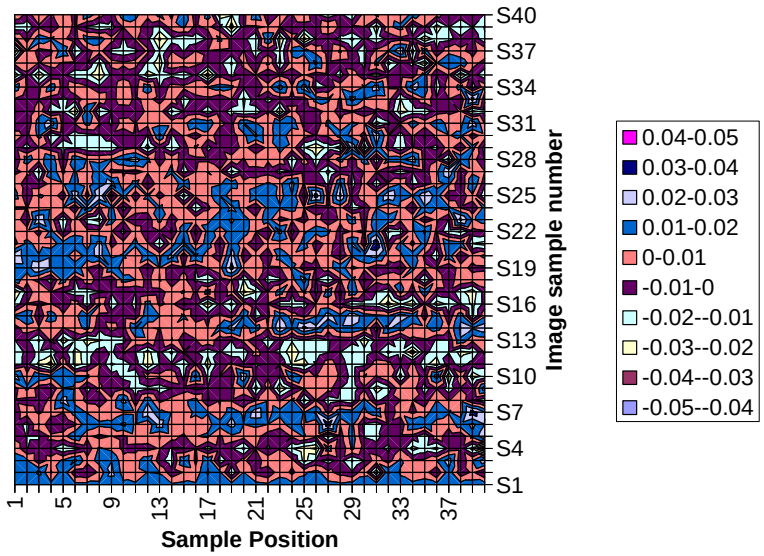


Figure 4-5 – Variation of multiple sample lines over time

Once the Canny filter is tuned and optimum Subpixel detection is obtained we turn our attention to measuring rigid body motion. Two methods are tested: the mean segment position method; and the segment intercept method. The vertical axis is split into an upper and a lower section of equal sizes. In the mean method, the mean position of each segment is measured as the average edge position. In the intercept method, a linear regression is calculated for a line fit

of each segment, and then the difference between the intersections of the line segments with the centerline is calculated. Additionally, calculations of slope for the two segments are made. Figures 4-6a and 4-6b show the variation of measured values over a 4 minute exposure. Figure 4-6a shows the stability of both methods over the test interval. Figure 4-6b shows the mean method data converted to nanometers. RMS values are given in both cases.

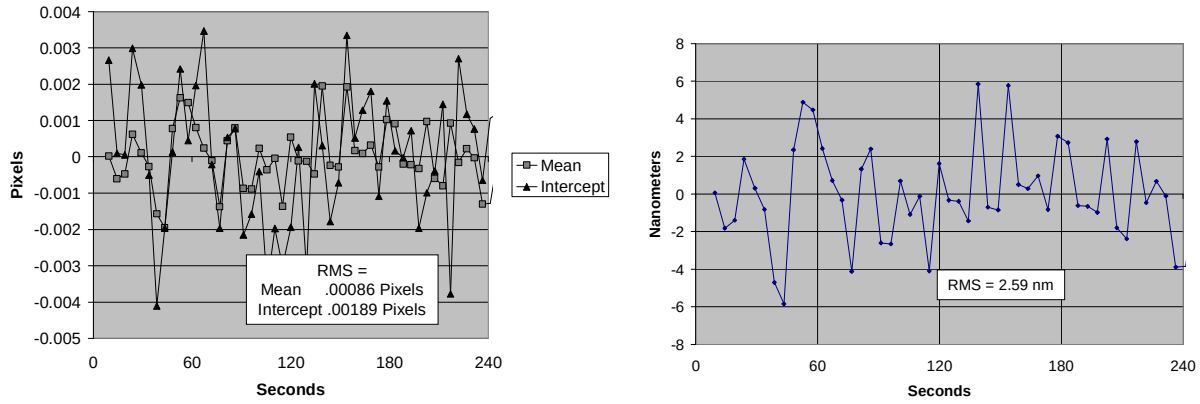


Figure 4-6 – a) Differential measurement stability – pixels b) – Equivalent nanometers

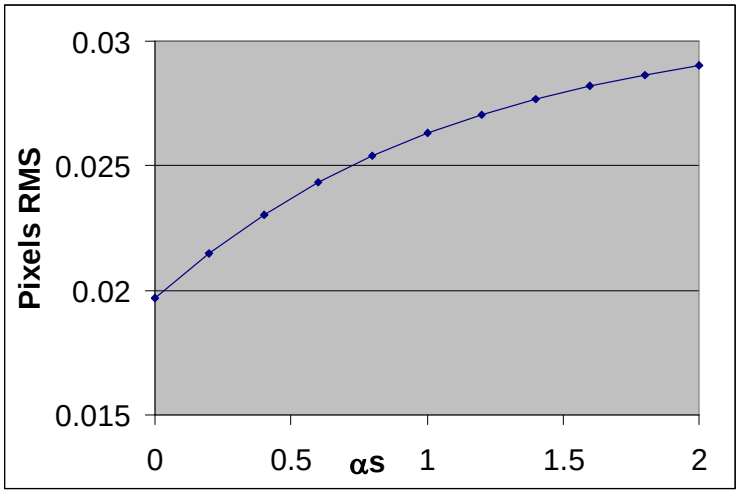


Figure 4-7 – Effects of α on error

Given a constant denominator in the Canny type filter we seek to find optimum values for as in equation 4-1. Empirically we can optimize as by the Laplacian error method described above. Figure 4-7 at right shows the Laplacian error in pixels for a typical image. α is varied from 0 to

2.0 in steps of .2 and the Laplacian error is calculated for each. We see that the operating error decreases monotonically as $\alpha$ is decreased to zero. This yields a degenerate form for the Canny filter which optimizes the sensitivity for our setup.

$$F[n] = \sum_{i=-k}^{k} \frac{x[n+k]}{2}, \qquad i \neq 0 \qquad \text{(4-4)}$$

## *Discussions*

The problem of edge localizations can be greatly simplified when the ability to control contrast and lighting is available. Under reasonably optimum conditions the best filter performance is seen to result from the simplest of filter structure. When samplings of individual pixels are combined, a resulting enhancement in object localization can be obtained.

It should be noted that the results given in this paper were obtained in an optics laboratory on the $7^{th}$ floor of a long slender 9 floor building. The major sources of uncontrollable errors typically came from building vibrations caused by elevator, personnel, wind loading, and physical plant. Most of these vibrations were observed to be in the range between 1 and .1 Hz. At these frequencies it was necessary to integrate multiple images to reduce the vibration noise. Experimentally, the noise levels were reduced by integration on the order of the square root of the number of samples. The best results published in this work were obtained with 64 image samples. Integration beyond this level was not attempted.

Gross long term building tilt was observed during several overnight exposures. Figures 4-8 and 4-9 give two different representations of long duration building effects. In figure 4-8 we see the effects of building tilt on the measuring apparatus. The video microscope was rigidly held by two clamps located about 4 inches apart. The long duration motion of the test article located 6 inches below the clamps is observed. A 1.5 pixel shift of the apparent target corresponds to a 5 micron drift in location equivalent to an effective tilt of the apparatus of approximately 100 nanoradians. The peak displacement also occurred near lunar noon suggesting that this tilt is related to tidal forces.

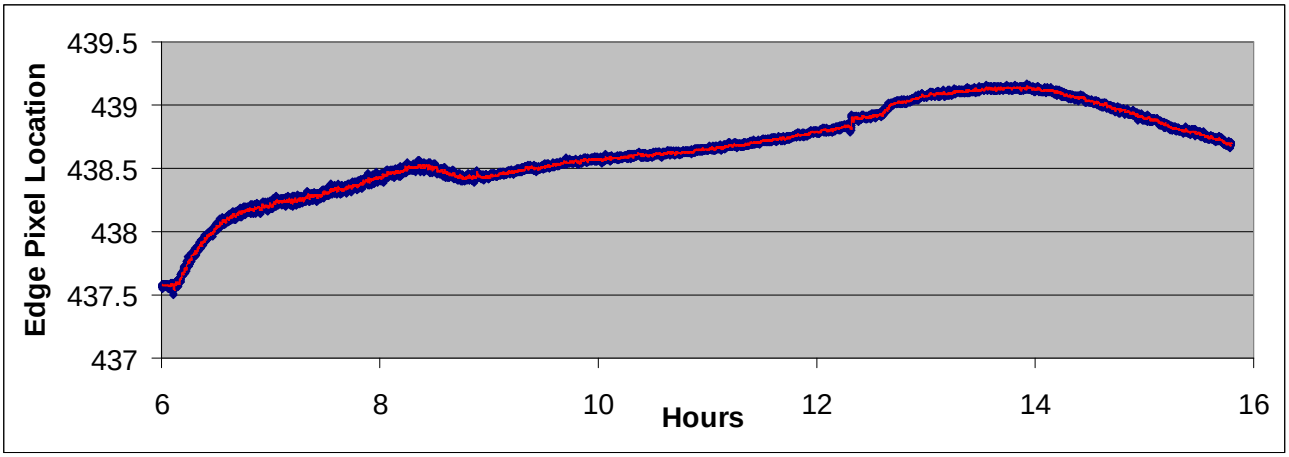


Figure 4-8 – Long term lateral drift caused by building motion over 10-hour exposure

Figure 4-9 shows the short duration measurement excursions. The graph presents a long term picture of variation of the range of observations over discreet 30 second periods of time. Variations from 6:00 hours till 9:00 hours are predominantly due to motion of people in the building. These decreased noticeably after 9:00 hours when the building was vacated. An interesting spike occurs near midnight and is attributed to an unknown function of the building's engineering plant.

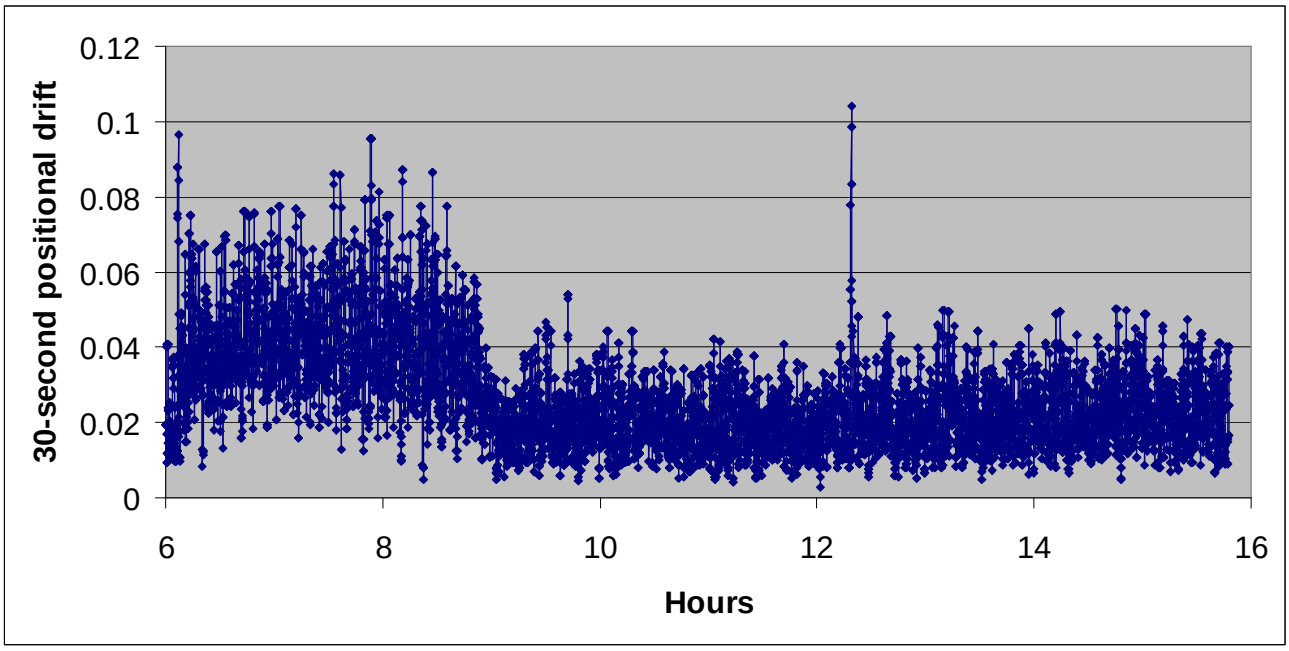


Figure 4-9 – Relative building vibrations by position excursion magnitudes over 30 second moving window

## *Conclusions*

In conclusion, we find that a well designed subpixel detection system can be extended to a desired degree of accuracy by oversampling alone. This method is limited by the availability of image real estate and the size requirements for individual subpixel measurements. The individual subpixel sampling regions are optimized when the filter kernel is nearly the same width as the Gaussian blur region of the imaged edge. This sets a practical limit on the number of edges which can be located in a single image. When these factors are optimized, experimental results have shown that nanometer target localization can be attained.

The Laplacian noise metric is seen to be a viable quantitative method for filter optimization when imaging methods exceed the edge irregularity of the chosen target. Under video magnification, the best commercial etched chrome on glass targets possess edge irregularities larger than the resolving power of a .01 pixels Canny filter. Under these circumstances, the Laplacian noise metric becomes a powerful tool for comparison of edge detection filters by effectively ignoring the local irregularities of the target.

Because adjacent edge measurements consist of partially correlated errors, the improvement in accuracy of mean values is only improved by a factor of the cube root of the number of samples. The use of multiple lines produces an uncorrelated error distribution which improves with the square root of the number of lines placed on the rigid target. When properly combined we have demonstrated the ability to localize rigid target to nanometer scale accuracy.

# 5 – Experimental Results and Model Verification

## *Introduction*

In chapter 2 we developed a mathematical model describing the effects of divergence on the Goos-Hanchen (GH) shift for plane waves. We refined Artmans[3] classical description of GH shifts by introducing a mathematical representation of the effect of natural source divergence of plane waves caused by nonideal sources. In this chapter we present experimental results which confirm the proposed model using bench top apparatus.

Experimental results show the symmetrical response curves for the edge shift function described in chapter 2 (equation 2-15). Imaging interpretation is guided by the convolution expressions presented in chapter 3 and precision is obtained using the image processing methods presented in chapter 4. The combined synthesis of methods results in processed data which validates the predicted mathematical and numerical models for edge shift, divergence dependence, and spatial dispersion. A statistical error analysis shows the improvement in precision of the mean position method versus the slope intercept method for analyzing the images of Ronchi grating internally reflected off coated and uncoated surfaces of a fused silica prism.

In this chapter we also present a detailed analysis of the types of errors encountered in the experimental process and the methods used to correct and or compensate for each source of errors. In light of error sources we discuss practical consideration for several methods of physical setup of the experimental apparatus. The relative merits, limitations, and benefits of

each setup is considered in the determination process for optimizing the precision, accuracy, and sensitivity of the ultimate experiment

## Experimental setup

The optical setup of this effort, as shown in figure 5-1 and figure 3-6, consists of three major parts, the light source and collimator, the grating and rotatable prism, and the imager with video microscope lens. An additional image acquisition and image processing system completes the total setup providing the platform for acquiring the video stream and measuring the observed shifts through custom written image processing routines

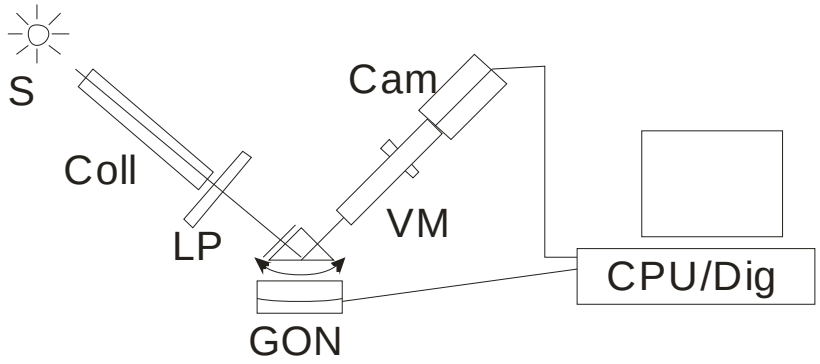


Figure 5-1 Experimental setup.

For our testing the video microscope and imager are fixed components. The camera/lens combination is mounted on a video microscope platform and the only control is the focusing knob. The ccd-imager is an Edmund Optics E03BW monochrome 1/3 inch CCD imager with a 50dB SNR. The lens is Edmund Optics V-300ZM video microscope with a fixed focal distance operated at a 3X zoom setting. This provides a working pixel size of nearly 3 microns in the image plane.

The light source and collimator part of the optical setup has been tested for three different collimator configurations. The light source is a Kratos LH15071 with a 200W Xenon lamp installed. To provide monochromatic operation the light is filtered through a .650 nanometer interference filter with a bandwidth of 11 nanometers. This provides a deep red light which operates in the region of maximum sensitivity of the ccd-imager and provides adequate wavelength to obtain measurable shifts. The lamp normally is mounted with an aspheric collector lens and focusing assembly which is removable. Different lamp configuration both with and without the collector lens were tested to identify the best lamp setup to maximize intensity and collimation at the reflecting surface of the prism.

The collimator section of the optical setup was the most challenging to optimize. In theory the best collimation should be obtained by focusing the beam through a pinhole (see figure 5-2) and collecting the spatially filtered light at an appropriate focal distance beyond the pinhole.

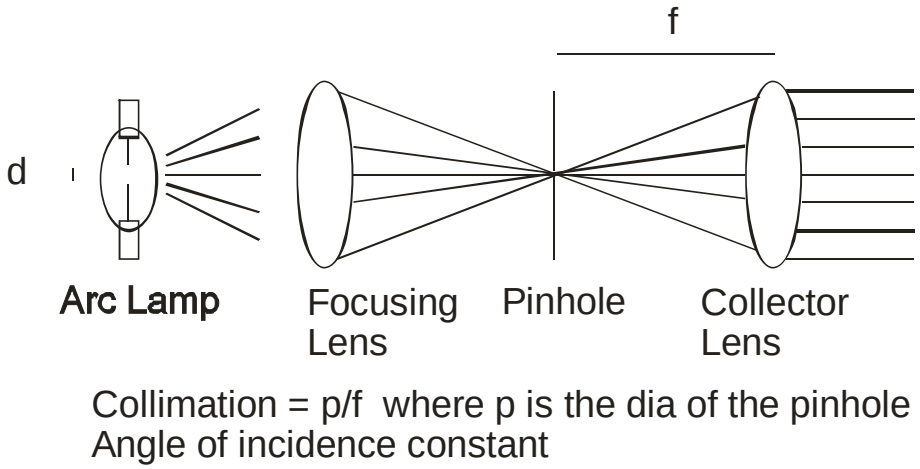


Figure 5-2 Collimation enhancement by introduction of pinhole spatial filter.

The introduction of a pinhole at the focus point of the relay lens allows a working reduction in the diameter of the apparent source. In practice this produced excessive diffraction effects that interfered with the Subpixel processing routines by radically varying the brightness and contrast

along the imaged lines of the Ronchi ruling. Alternately, the collector lens was removed from the setup in figure 5-2. A long focusing lens was then used and the pinhole to target distance was increased to limit the angular spread at the grating. This method allowed for line averaging of shifts with a slight loss in measured shift near the critical angle.

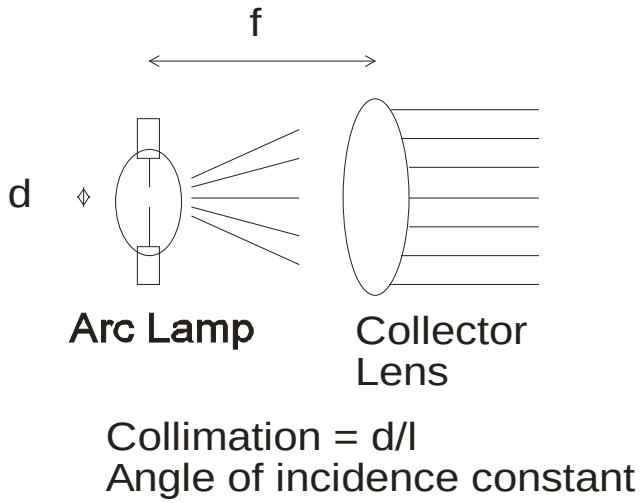


Figure 5-3 Collimation by collector lens. The degree of collimation is determined by the size of the lamp arc and the focal distance of the collector lens.

An alternate approach was to remove the collector lens from the front of the lamp housing and either collimate through an external collector lens (see figure 5-3) or merely use the uncollimated light at a sufficient distance to produce an effective collimation ratio of arc size to working distance (see figure 5-4). The former approach tends to produce more luminance at the image plane. Another difference between these two methods is that a collected collimation produces uniform shift over the entire image area whereas an uncollected point source distributes the angles of incidence uniformly over the image area.

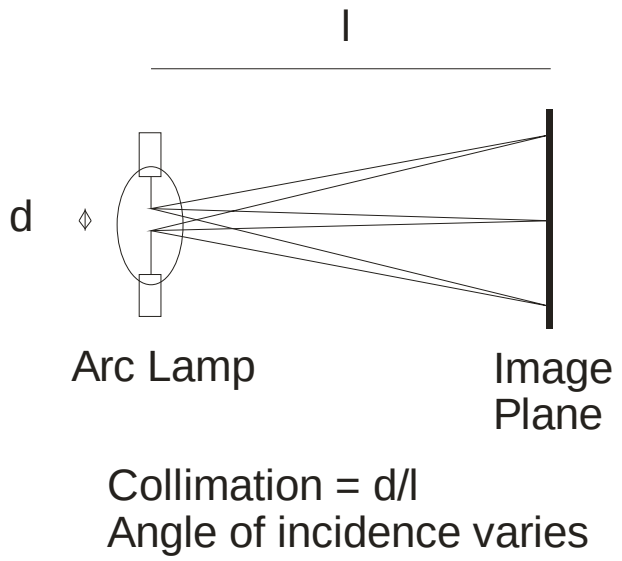


Figure 5-4 Collimation of arc lamp used as point source. The collimation is determined by the size of the lamp arc and the distance to the image plane

The collected method requires scanning the prism through a range of angles to obtain a range of delta angles but provides multiple samples which significantly reduce the variance of the sample mean. The uncollected source methods requires careful alignment of the prism to the critical angle but provides a broad spectrum of angular alignment methods to be obtained from a single image reducing the errors that arise from inaccuracies in the discrete positioning of the goniometer.

The other section of the optical setup is the grating and prism section. The prism is placed between the imaging system and the Ronchi grating. Because the lens is a fixed focus and nontelecentric, focusing on the grating causes the line between the coated and uncoated surfaces of the prism to be blurred. The severity of this blur is a function of the distance from the grating

surface to the reflecting surface of the prism. Minimizing this distance optimizes the operational range available in the image for processing but physical limitation dictate certain restrictions.

The prism is mounted above the goniometer at a distance where the axis of rotation coincides with the reflecting surface of the prism. Additionally, to avoid focal plane shifts under rotation, the centerline of the imaging axis must cross as close as possible to the axis of rotation. Otherwise, the focal plane will shift significantly requiring continuous refocusing of the system. Focal control was found to be crucial to obtaining precise results. This geometrical requirement sets a minimum distance from the reflecting surface to the grating surface equal to greater than half the square dimension of the prism. In our setup the interference with the physical mount of the prism further increased this distance. Despite these problems, we were able to reduce the blur to manageable levels. Future setups can benefit from better mounting designs and the use of smaller prisms.

In addition to the physical setup, there is an image acquisition and image processing system which is crucial to effective measurement and analysis of the results produced by the optical instruments. Image acquisition is accomplished by use of a Matrox Meteor II video digitizer. The digitizer reads the analog video stream, in RS170 format, and converts the data to 8 bit digital image data. High level control of the digitizer is performed by the Active MIL-Lite™ software commands programmed into the custom designed operating software. The MIL-Lite™ functions control initialization of the digitizer system, image capture control on the video stream, and basic extraction of individual pixel information.

The total system is completed with a custom developed image processing software package written in Visual Basic. The Visual Basic platform contains a vast array of linkable object modules and is ideally for rapid prototyping. It also provides a simple and quick capability for implementing visual control functions and allows direct access for image display, interactive mouse control, control buttons, file handling, as well as a myriad of other useful tools.

## *Noise analysis, correction, and/or compensation*

Now that the experimental setup has been described and before we discuss experimental procedures, it is instructive to first describe the various sources of systematic and random errors in the apparatus. Noise arises from many sources which are classified as either random or systematic. Random sources include dirt on the optics, vibrations of the apparatus, electronic noise in the imager and digitizer, and irregularities in the optical components. Systematic sources include optical diffraction, focal control of the imaging system, and alignment of the optics.

### Random error sources

Cleanliness of optical components is absolutely necessary when working with optical imaging systems and image processing systems. In our case, simple cleaning of all optical surfaces with mild cleaning agents such as water and isopropyl alcohol was insufficient to adequately reduce surface contamination. The imaging system was used with an object plane pixels size of 3 microns and any residue was visible in the image. The image processing system was designed to resolve single edge positions to .015 pixels or 45 nanometers. Hence careful cleaning with

acetone was required. Large dust particles which tended to settle on the surfaces was removed with sprays of compressed air. An example of the effectiveness of these methods can be seen by comparing figure 5-5 and 5-6 which are examples of alcohol cleaning and acetone cleaning.

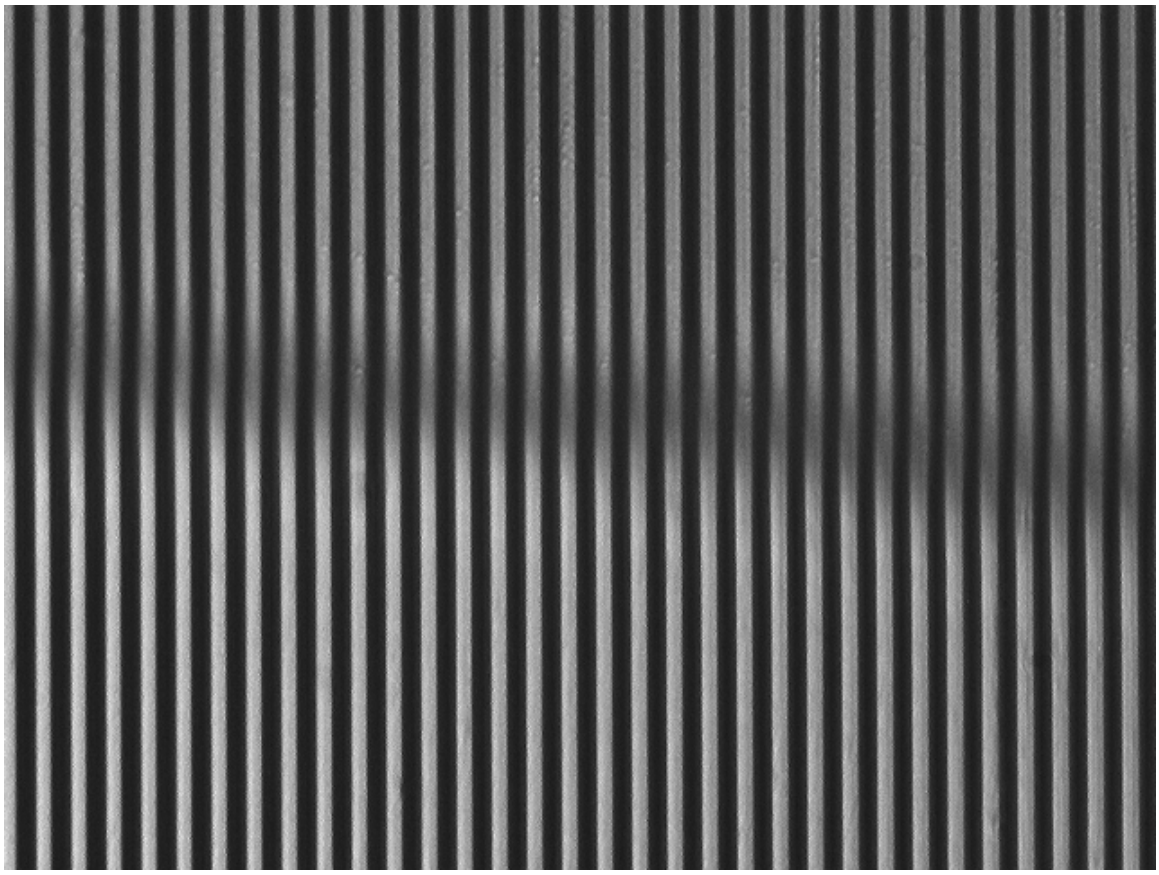

Figure 5-5 Alcohol cleaned grating

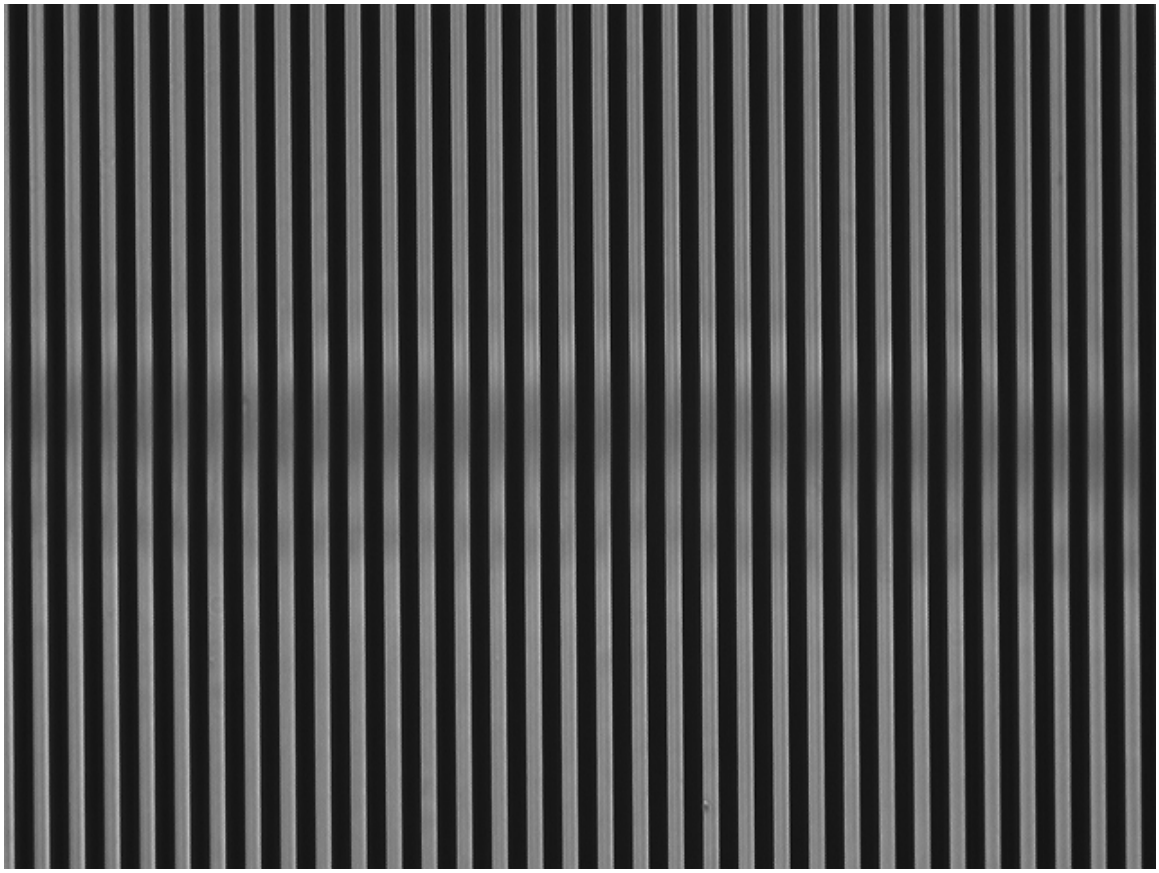

Figure 5-6 Acetone cleaned grating

Vibrations effects were previously studied during the image processing development work presented in chapter 4. For the final operating software an image integration capability was implemented to provide the user with the ability to integrate multiple successive images up to a maximum of 64. In normal operation, 16 image integration was used as default. This had the additional effect of reducing the electronic random noise arising from the imager chip and the digitization process.

Fixed errors

Irregularities in the optical components are a fixed property of the components. They are determined by specifications at time of purchase and hence a measure of control is possible. For

the prisms, a specification of l/10 for flatness and 10/5 scratch dig was used. The prism coating was performed by a third party vendor using vacuum tape for masking of the uncoated prism surface area. The limit of edge roughness was thus determined by the quality of the masking tape. The Ronchi grating were off the shelf gratings produced by UV photo etching and specified to be straight and spaced to 1 micron. In practice the edge roughness is determined by the quality of the UV mask and the consistency of the photo etching process.

### Systematic error sources

Diffraction was a significant source of noise early in our measurement cycle. The use of pinhole apertures created severe diffraction effects which eventually forced us to abandon the spatial filter method altogether. Diffraction caused by the rulings on the Ronchi gratings could not be eliminated but was reduced by careful control of focus and by maintaining adequate illumination intensities. Figure 5-6 above shows a well controlled diffraction condition. The faint dark vertical stripes are diffraction from the ruling lines. If they are faint enough the Subpixel image routines essentially ignore them and they have minimal impact. Surprisingly, they have a beneficial role in helping the operator identify optimum focusing. As focus shifts, the lines appear to move towards or away from the edge. When the first diffraction minimum is equal in size to the diffraction line spacing, focus is optimized. An example of problematic diffraction is seen in figure 5-7 which was obtained using pinhole collimation.

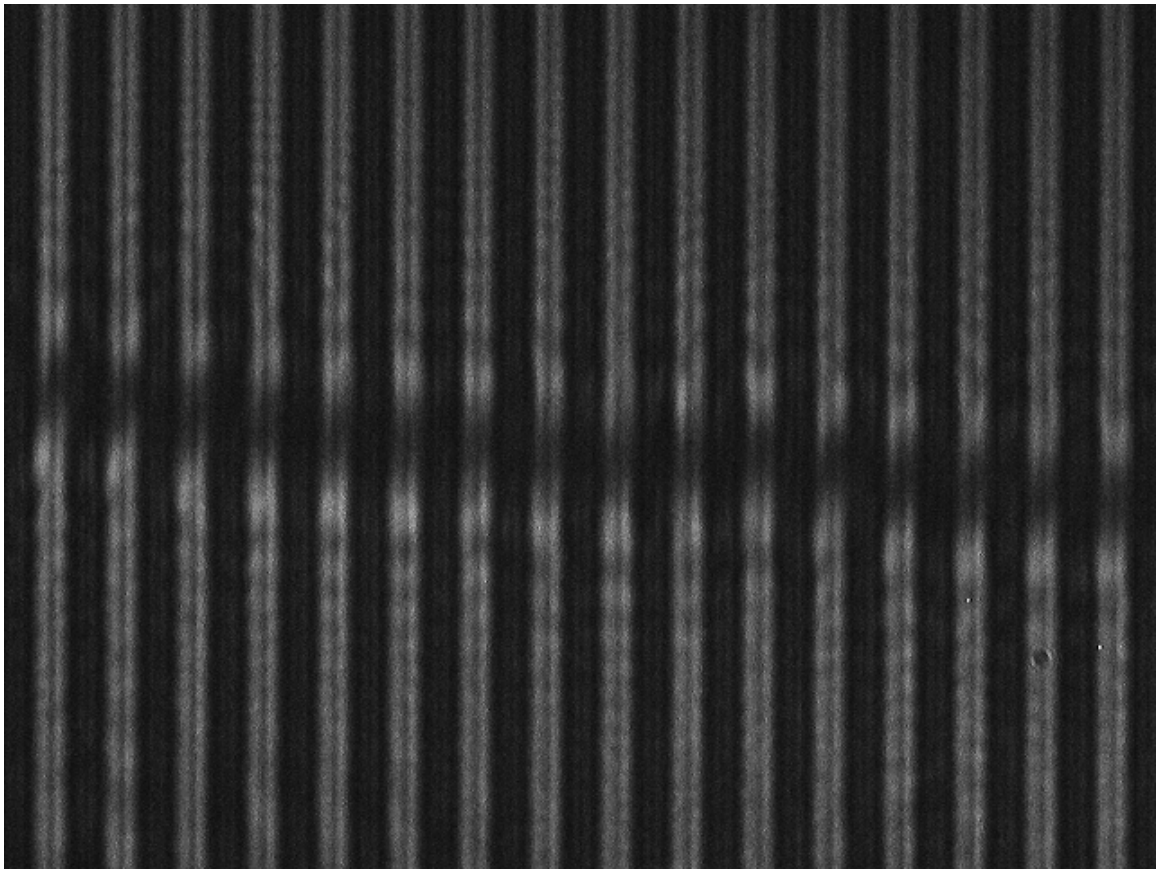

Figure 5-7 Diffraction effect from pinhole filtering

Here we see distinct refraction lines in both the vertical and horizontal direction. The horizontal diffraction indications arise from the reflective coating edge on the prism and provide sufficient contrast noise to severely reduce the precision of the Subpixel software routines. A close inspection of figure 5-6 reveals the existence of the horizontal diffraction lines at a significantly better compensated level.

The resolution of the edge detection software is sufficient to reveal the figure of the individual edges. The edge figure reveals components of both random and systematic error and permits the implementation of systematic error compensation. Best results are obtained when the edges are aligned as close to vertical as possible. The random effects of edge irregularities are avoided

when mean line segment is measured as opposed to slope intercept measurements (see chapter 4). In the former case local variations which are randomly positioned on a typical sample line are merely averaged out whereas in the latter case the location of the irregularity adversely affects the slope calculation and is dependant on the location as well as the magnitude.

Figure 5-8 is a graph of one measured edge. The edge shown here contains a segment of coated surface separated from a segment of uncoated surface separated by the blur zone resulting from the focal blur at the prism surface It can be seen that the edge locations transitions smoothly from coated to uncoated sides indicating that the blur is uniformly distributed and diffraction effects are minimal. In cases where diffraction effects were noticeable the blur transition edge profile took on an "S" shape curve, first rising then falling and rising again at the other side. A minor diffraction effect is seen in figure 5-8 between the horizontal positions of 150 and 200 pixels.

This problem is compensated for by excluding the blur and diffraction zones from the statistical regions of interest along the line profile. This is accomplished at run time by operator identification of the transition zone in the live image.

Scrutiny of figure 5-8 reveals features which can be attributed to physical edge roughness as well as to precision of the Subpixel routine. In general, more localized the variations are closer they are related to the Subpixel precision. Broader the shape of the variations from straightness, more they are related to the true shape of the grating edge. For this reason we use the Laplacian discriminator described in chapter 4 to determine the precision of the edge locating process and

we use RMS deviation from a line fit to determine the edge roughness of the grating. Skew of the line then becomes an estimator of line straightness.

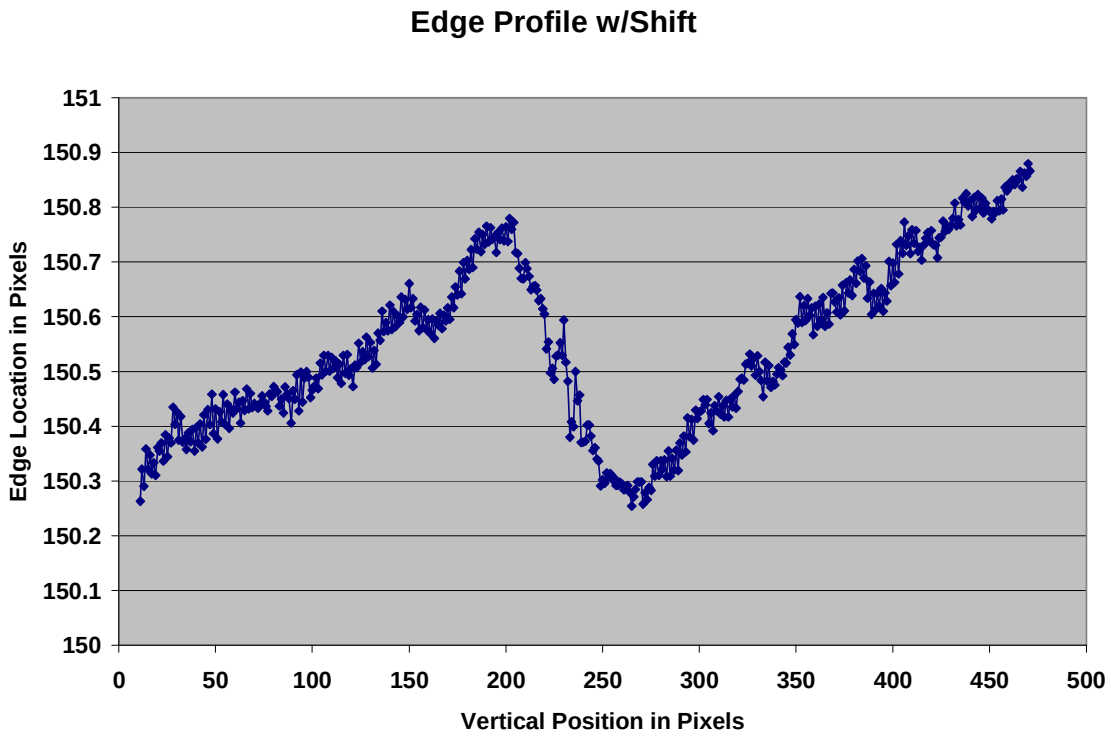


Figure 5-8 Edge profile of a typical sample line

The final source of systematic error is focal control of the imaging system. In normal edge detection algorithm a small measure of defocus is generally desirable. In GH studies the dispersive property of the shift can be disrupted by defocus. Best results are obtained when the coated edge reflection is kept in sharp focus. This technique separates the Gaussian blur effects from the GH dispersion effect allowing for more accurate and precise shift measurements.

## *Experimental procedures*

General method

The general technique of obtaining a shift reading involves measuring the relative location of edge positions along regions which are reflected by the coated surface and regions which are reflected by the uncoated surfaces. Precise edge locations are determined by the Subpixel algorithms in the processing software. Coated and uncoated regions are manually identified by the operator during the software setup process which identifies the overall region of interest in the image and the diffraction blur exclusion zone.

Line profiles are digitally obtained by software tracing of edge positions along the identified edge. If multiple grating lines are contained within the region of interest, then multiple tracings are performed and the results are stored in array fashion. Once the tracing is completed, segmentation is performed to separate line segments from lines. Statistical analysis is performed on the line segments to obtain mean line position and linear regression line analysis. From the linear regression information, projection of upper and lower segments can be made to the midline position in the exclusion zone.

The projection shift measurement is then the positional difference between the projections of the upper and lower line segments to the midline location. For the mean position measurement, the uncorrected shift is the difference between the mean centers of the upper and lower line segments. Projection shift measurements are sensitive to the straightness and uniformity of the

line segments. Mean position measurements must be compensated for tilt of the lines to the vertical direction of the image

Once the individual line shifts are measured they are stored to disk as shift measurements for each individual line within the ROI. Additionally, a statistical mean of all lines with the ROI is calculated and stored to disk. Storage is done to a file written in Excel readable comma separated variable (CSV) format. If desired, the individual line profiles can also be stored to a CSV format for further dissection. This is the source of the data graphed in figure 5-8.

### Scanning for variations in incidence angle

Two different methods are used for varying incidence angle depending on the type of collimation used. The simplest is the uncollimated point source method shown in figure 5-4. In this case the individual sample lines have differing angles of incidence related to the physical separation of the lines on the grating and the distance to the source. As a result they produce observable shift differences from line to line which are modulated by the angle of this prism. By adjusting the prism tilt until the maximum shift occurs, a centered shift curve can be obtained. The advantage of this method is the ability to obtain a shift versus incidence angle relationship from a single snapshot. The disadvantage of this method lies in the inability to filter out noise from individual lines on the Ronchi grating. An alternate approach, as previously discussed, was to place the Ronchi grating at a sufficient distance from the source focal position to minimize the angular spread at the grating plane. This allowed for line averaging with minimal loss of accuracy except when the critical angle fell within the imaging area.

The second scanning method deals with sources where the collimated light is collected in parallel rays. In this case the incidence angle is completely controlled by the angle of the prism. All lines in each snapshot are indicative of the same angle of incidence. Angle of incidence is then controlled by rotation of the prism between snapshots and careful recording of the goniometer position is required. Uniform stepping of the goniometer between snapshots aids in providing uniform increments on angle of incidence. Goniometer step size is calibrated by making angular readings on the micrometer at known angular settings of the goniometer.

As the prism is rotated the blurred image of the coating edge will shift laterally. If the coating edge is not square with the grating lines this may cause a working shift in the required exclusion zone. When this shift occurs, the operator must recognize the effect and recalibrate the exclusion zone manually. The software provides the mechanisms for performing this task between snapshots.

### Special considerations

Since the edge shift models predicts symmetry about critical angle, it is best to insure that the scanning range of incidence angles is relatively symmetrical about the critical angle. This requires an initial scanning cycle to locate the critical angle on the goniometer. If no changes are made to the collimator setup, the critical angle setting on the goniometer will remain constant and can be used repeatedly. If changes are made to the optical setup, the centerline must be reestablished.

Focal quality plays a large role in controlling the precision and accuracy of the experiment. Rotation of the prism alters the path length between the camera and the grating under the best of conditions. Tilt of the grating to the optical axis of the imaging system creates nonuniform focus across an individual image. Careful design and alignment are required to minimize these effects. Refocusing between angular settings is virtually essential for angular ranges in excess of a fraction of a degree.

In our experiments the camera and lens are mounted with a fixed axis which cannot be adjusted when the prism is rotated. Hence the illumination axis is not in alignment with the viewing axis. This sets a working limit on the amount of angular variation of the prisms that the camera will tolerate to main adequate brightness. This also set requirements on the alignment of the camera to the critical angle. In practice, a fused silica prism was selected to provide a critical angle close to 45 degrees so the imager could be pointed with a 90 degree square mechanical setup. Results have shown, this allows us more operating range below critical angle than above critical angle.

A second method of confirming the theoretical predictions of the models is in demonstrating the dispersive nature of the GH shift for divergent beams. Of all the tests this is the most difficult because the dispersion effect is very similar to the Gaussian blur of the imaging system. Since we are looking for a blur difference between the coated and uncoated reflections, we must bring the coated reflection into near perfect focus to observe the dispersion of the uncoated reflection. We must also avoid interference with the diffractions lines while taking these

measurements. In the results section we will present two successful measurements and discuss the difference between them.

## *Experimental Results*

Experimental results are the foundation of confirming theoretical predictions. The validity of a model frequently is based upon consistent and repeatable laboratory demonstration of model predictions. In our effort this is accomplished by two independent demonstrations.

The first demonstration and perhaps the most difficult is observation of the dispersive nature of the divergence model. The line spread function given in chapter 2 predicts that a dispersive wave with a known angular distribution of components will experience dispersive shifts in proportion to the distribution of energy across the angular spectrum. This is described by an impulse response curve. In chapter 3 we saw that the observable quantity seen by an imaging system becomes the convolution of the impulse response with the step or slit aperture.

The second demonstration is the prediction of the minimum shift, or edge shift function. The minimum shift occurs for those components of the incident wave which have the greatest deviation from critical angle thereby establishing a leading edge to the impulse response. The edge detection algorithms used in this work detect the position of maximum slope along the transition from light to dark. Edge slope maximum has been shown to occur at the point where the impulse response reaches maximum value. The relation between edge shift and peak shift has also been shown to be reasonably constant within a few divergence angles of critical angle.

Dispersion observations

All normal imaging systems produce a natural edge blur with a Gaussian distributed intensity profile. The degree of blur is described in optics by the modulation transfer function of the imaging system or MTF. The higher the MTF the less apparent the blur becomes. The MTF is a then a measure of the best edge focusing capability of a particular lensing system.

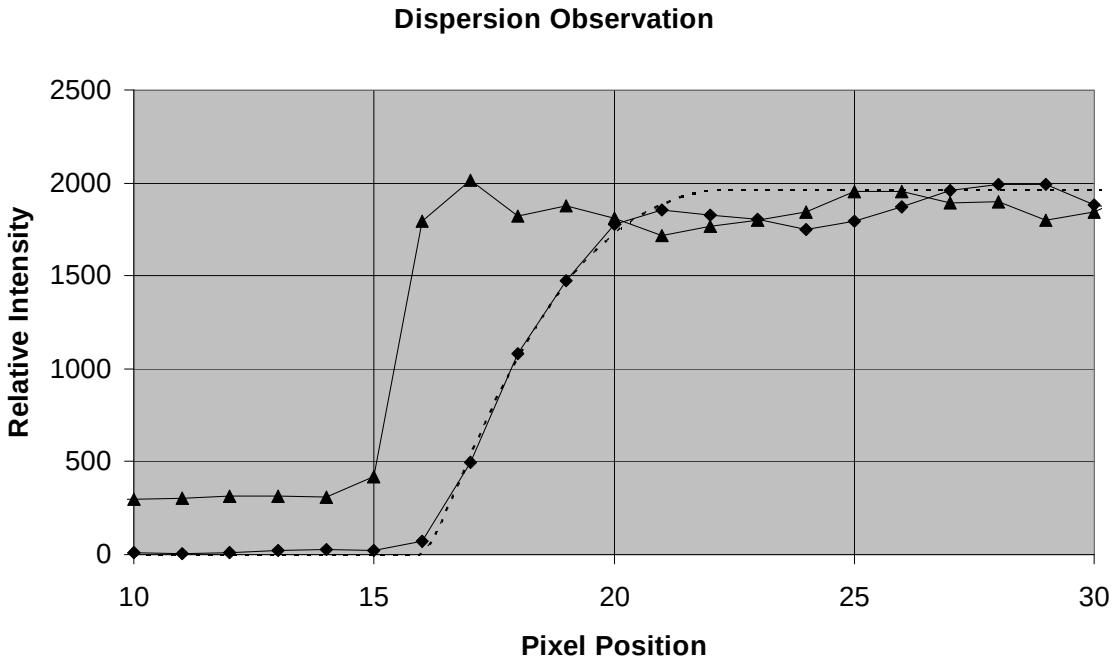


Figure 5-9 Edge shift dispersion. Triangle symbols are unshifted profiles, diamond symbols are shifted and dispersed profiles, and dashed line is the model prediction for shifted dispersion.

Figure 5-9 shows a simultaneous intensity recording of two sample lines oriented across the edge under study. The nearly rectangular intensity profile shown by the triangle markers is from a coated section of the prism's reflective surface and shows the minimum edge blur obtainable

with our lens. More than 90% of the intensity transition occurs within one pixel of the edge location for both the leading and trailing edges. The smoothed intensity profile identified by the diamond markers shows the reflection profile from a section of the uncoated area of the prism. Visual inspection shows that the theoretical dispersion prediction of the model correlate very well to measured shift/dispersion profile. The difference between the shifted and unshifted profiles is indicative of the dispersion encountered by the internal reflection at the uncoated surface. The pixel position is in reverse order to account for the inverting nature of the lens system. The waviness of the profiles at high intensity is caused by the diffraction induced at the grating line edges. Although the dispersion is clearly visible on the leading edge, the presence of a diffraction peak near the trailing edge obscures the dispersion signature expected at the trailing edge.

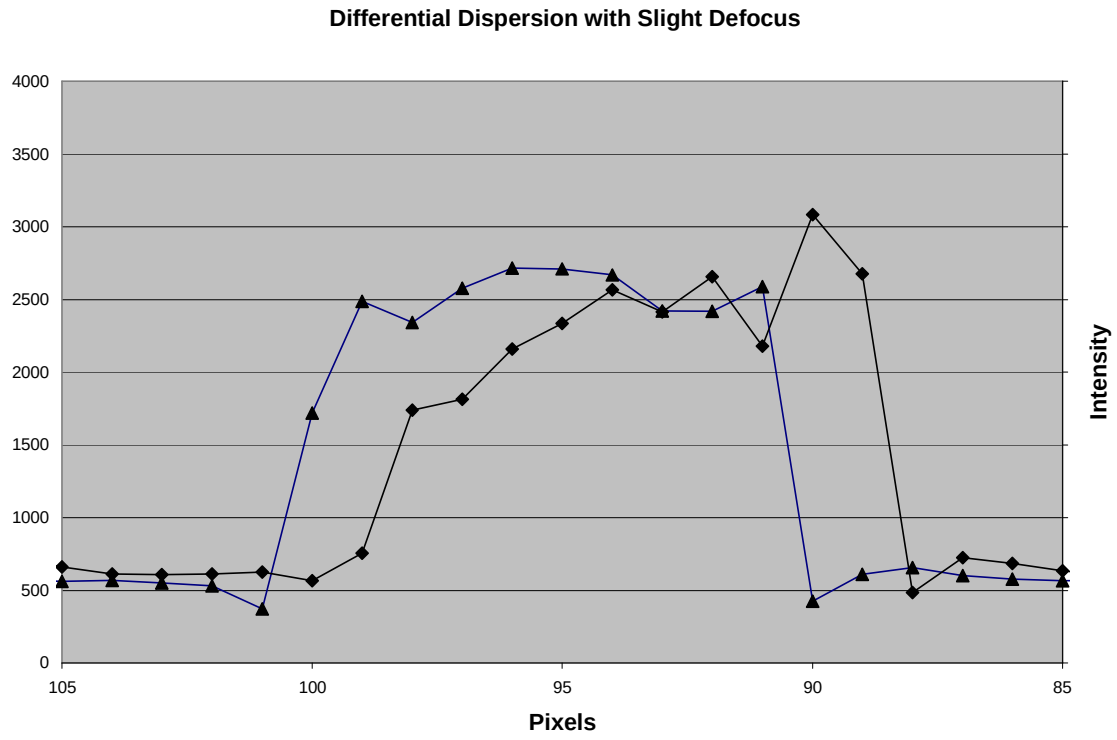


Figure 5-10 Dispersion at slight defocus.

Figure 5-10 shows the degradation of the dispersion signature when the image is slightly defocused. The triangle marked line shows a rise distance of two pixels and the shift in the diffraction lines partially obscures the dispersion intensity profile. Note that the coated edge reflection has a more dispersed rise profile and that the uncoated edge reflection is clipped by a local diffraction minimum.

Edge shift measurement results

Three different methods for measuring edge shift as a function of incidence angle were investigated. The first method involved using an uncollimated point source and allowing the natural divergence of the point source and the distance to the target to control the divergence (see figure 5-4). The results were highly sensitive to grating line irregularities and large errors were seen.

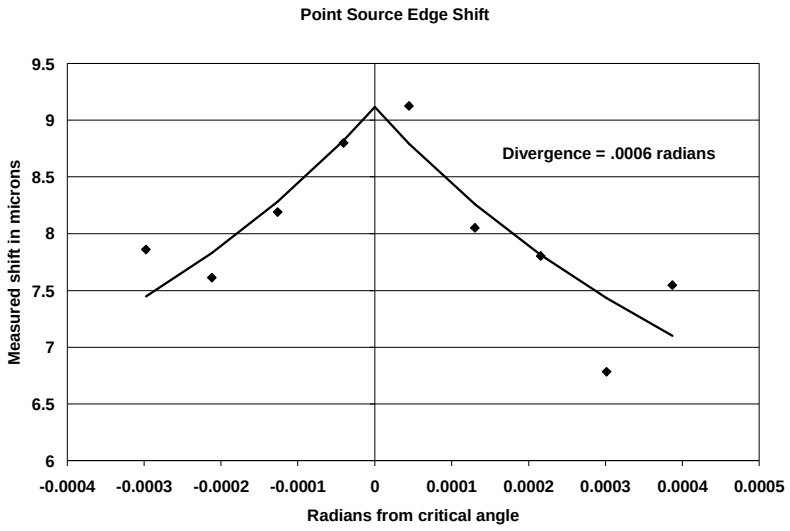


Figure 5-11 Point source edge shifts with fixed variation of angular deviation. Solid line with no markers is the model prediction. Diamond symbols are the measured data.

In figure 5-11 we see the results. A divergence of .0006 radians was observed by a standard error of approximately .3 microns was measured. The large error is attributed to the single sample nature of the data and the inability to remove individual line irregularities as previously discussed.

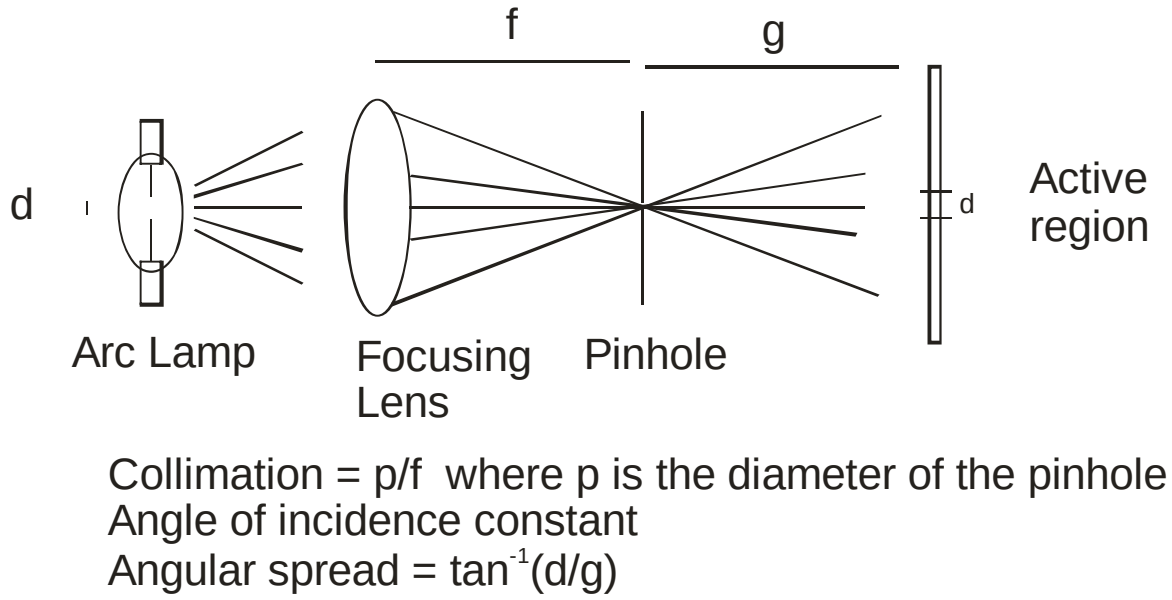


Figure 5-12 Modification of pinhole collimation method without collector lens

The second method of measuring shift as a function of incidence angle involve non-parallel rays such as shown in figure 5-12. In the absence of the pinhole the divergence is determined by the arc diameter divided by the distance to the focusing lens. When the pinhole is present the collimation is reduced to the pinhole diameter divided by the focal length. The setup produces variations in angles of incidence across the grating and additional variations in angle of incidence are imposed by rotating the prism. By maintaining an adequate distance from the beam focal point to the grating angular spread can be controlled allowing multiple samples for each angle of incidence and significantly reduces the variance of the sample means at the expense of a loss in

divergence angle. Once again diffraction effects and low light levels necessitated removal of the pinhole.

The results shown in figure 5-13 were obtained using the setup of figure 5-12 with the pinhole removed. The number of sample lines per snapshot was 17 which theoretically reduce the standard error by a factor of 4.1. The corresponding loss in sensitivity was approximately a factor of 2.3 giving an overall experimental performance gain of nearly 2:1. The deviation from model predictions near the critical angle is the residual error caused by the angular spread of the non-parallel rays.

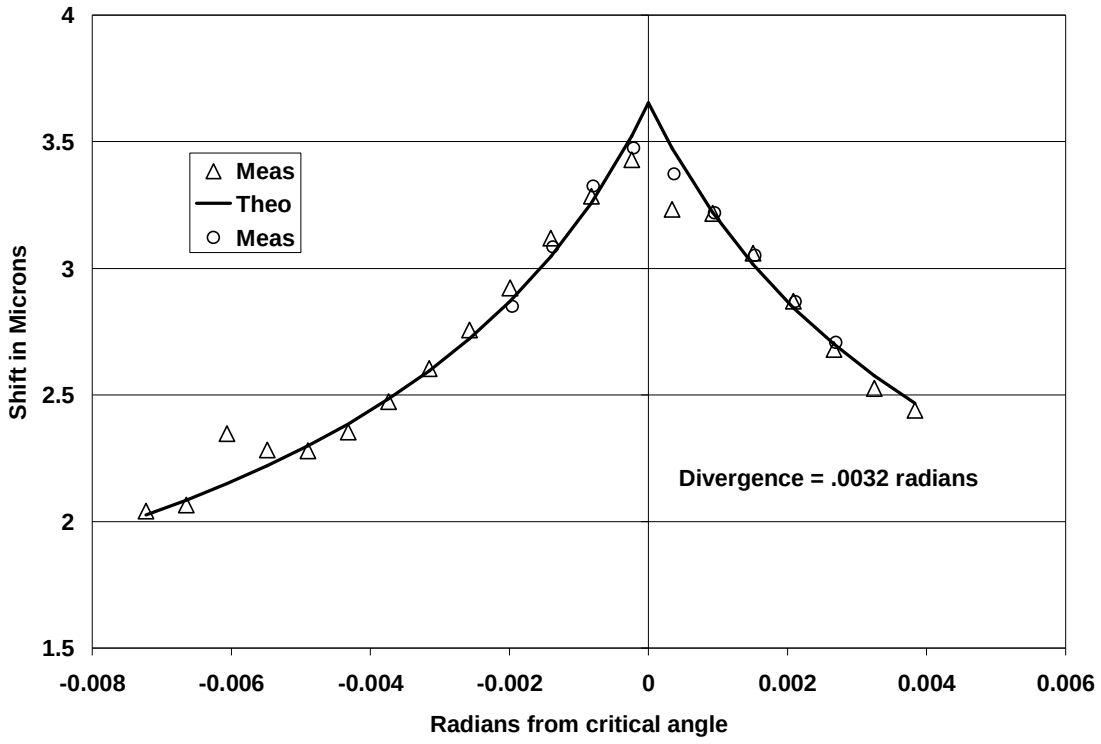


Figure 5-13 - Edge Shift versus alignment angle for uncollected light. Theoretical shift is shown by solid lines. Two sets of measured data are shown by markers only.

A visual inspection of figure 5-11 and 5-13 would accurately suggest that an error reduction of better than 2:1 was obtained. This is in fact the case because figure 5-12 includes additional gains obtained by differences between the slope-intercept and mean position methods of measuring the edge shifts.

The measured standard error of the slope intercept for the experiment of figure 5-13 was 171 nanometers. The standard error of the data shown in figure 5-13 was 80 nanometers for the complete dataset and could be reduced to 31 nanometers by removal of the 4 apparent outlier points compared to a standard error in figure 5-11 of 331 nanometers. For proper disclosure we present the full dataset in figure 5-13.

The third set of measurements was made with the setup of figure 5-3 and is shown in figure 5-14. Distance from lens to source is one half the focal length of the lens. This configuration was tested at multiple focal lengths and the divergence results were correlated to produce a working estimate of the lamp's arc height.

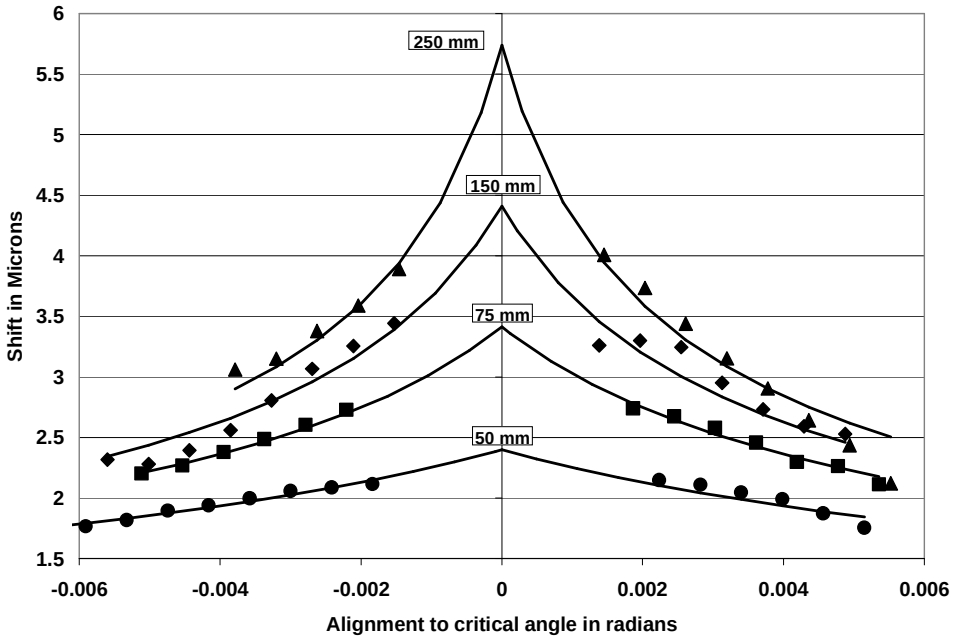


Figure 5-14 - Multiple divergence tests showing array exclusion zones

It was found that this configuration produced very good correlation to model predictions in regions away from the critical angle. Values of shift near critical angle were lower than model predictions and the width of the exclusion zone increased with shorter focal lengths, i.e., higher divergences.

Figure 5-15 shows the same tests with the data from the exclusion zone included. The shift data dips from the inverse square model near the critical angle. One area for further study is to explore and quantify further the cause of this behavior.

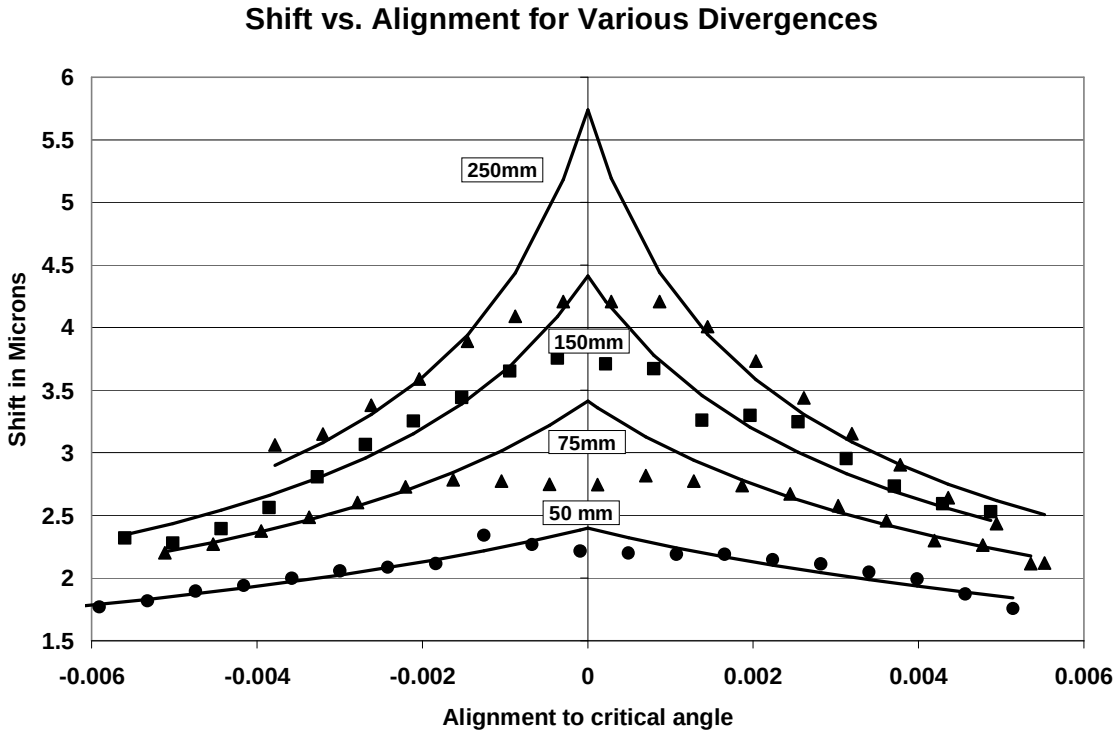


Figure 5-15 – Multiple divergence tests with exclusion zone measurements

The precise cause of the central drop-off needs further investigation. It may be a result of the nonuniformity of the arc itself since our model is based on a uniform intensity profile. It may also be caused by crosstalk between adjacent slits which becomes more severe as critical angle is approached. The range of the exclusion zone does appear to correlate with the divergence angle, i.e., as the divergence is reduced the width of the drop-off zone decreases. In contrast the magnitude of the drop-off increases with decreasing divergence. Further study will be required to explain the nature of this drop-off.

The divergence results from the data in figures 5-14 and 5-15 can be verified for consistency. Since each test used the same source and the focal lengths are known, a linear regression is

performed between measured divergence and the reciprocal of the focal length. The resulting slope then becomes the arc length of the source. The results are shown in figure 5-16.

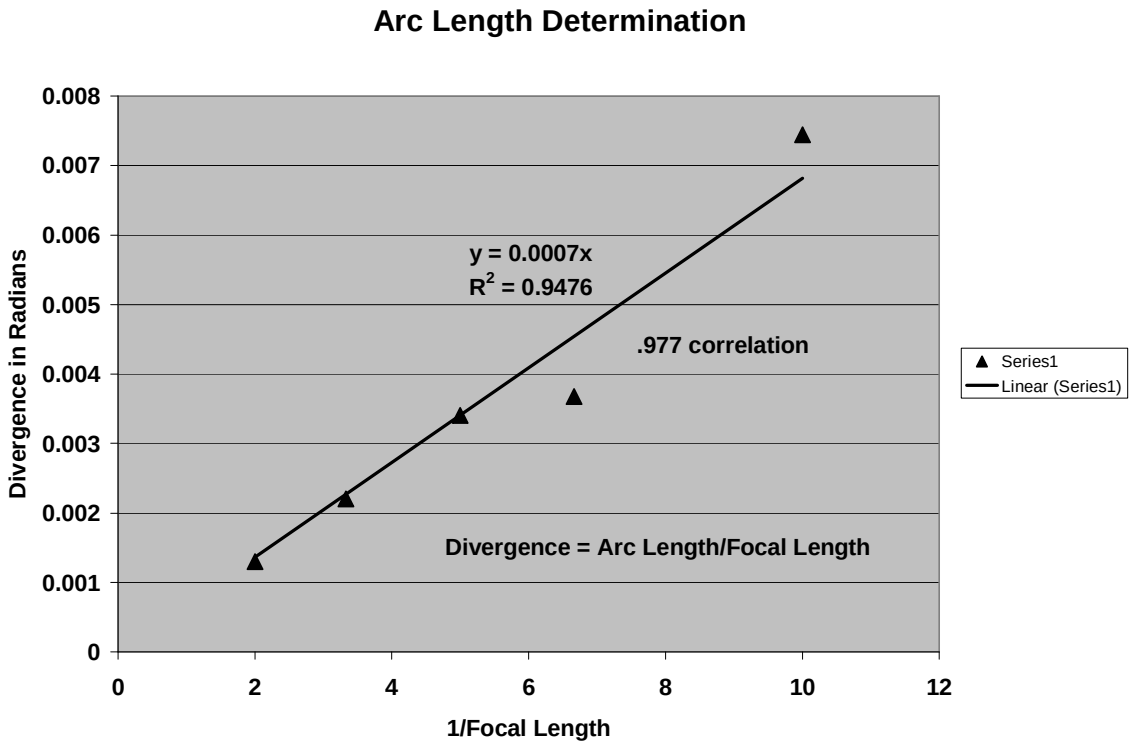


Figure 5-16 Arc length regression method

In this case with five different focal lengths the arc-size is found to be .7mm. Errors are most pronounced at shorter focal lengths with larger divergences.

## *Calculations and Error Analysis*

The basic scanning method provides statistical information about the observed shifts of individual lines of data. These lines are combined by simple averaging to produce shift data for each image snapshot. In the slope intercept method, the individual segments are reduced by standard linear regression method,

$$y_i = mx_i + b_i + \varepsilon ,$$

$$m = \frac{n\sum_{i=1}^{n} x_i y \; - \left(\sum_{i=1}^{n} x_i\right)\left(\sum_{i=1}^{n} y_i\right)}{n\left(\sum_{i=1}^{n} x_i^2\right) - \left(\sum_{i=1}^{n} x_i\right)^2}, \tag{5-1}$$

$$b = \bar{y} - m\bar{x} ,$$

where N is the number of sample points, x is the vertical pixel position on the line segment, and y is the measured subpixel position at the vertical position. The centerline position is then found by projecting the line to the center point. The shift becomes the difference between the upper projection and the lower projection,

$$\begin{aligned} y_c &= mx_c + b \\ Shift &= y_{upper} - y_{lower} \end{aligned} . \tag{5-2}$$

In the mean position method, the line segment center point is merely the statistical average of the subpixel measurements along the segment,

$$y_c = \sum_{i=1}^{n} y_i \Big/ n , \tag{5-3}$$

$$Shift = y_{upper} - y_{lower} - tilt .$$

In the mean position method we then have a relative shift difference which must be corrected for the mean tilt of the grating line to vertical. For individual snapshots the tilt is constant for all lines on the average. For multiple snapshots, the tilt may vary if the apparatus centerline changes, which may occur if the optical setup is bumped. The segment slopes from (5-1) and (5-2) are displayed after each snapshot analysis to provide the operator with an indicator of whether

the tilt of the apparatus has changed. In practice, the segment slopes are monitored and the tilt is uniformly corrected for all snapshots during extraction of the divergence angle.

The scanning measurement method when used with centerline method produces a set of data consisting of step positions on the goniometer and relative shifts between upper and lower segment mean positions. The unknowns in this data are the divergence of the source, the tilt of the grating lines, and the absolute position of the critical angle. Given a set of multiple readings it is possible to find all three unknown parameters using a least squares error method. The measured shift can be expressed as a function of the variables,

$$d_{meas} = \frac{\lambda}{\pi} \frac{1}{\sqrt{\cot(\theta_i)}\sqrt{\theta_d + |\delta_c + n\Delta\delta_m|}} + d_{tilt}, \tag{5-4}$$

where the d values are the measured shift and the tilt correction to the measured shift. The cotangent of the incidence angle is nearly 1 for the fused silica prisms. $\theta_d$ is the divergence angle, $\delta_c$ is the correction to the true critical angle and $\delta_m$ is the incremental tilt angle of the goniometer step size with n being the number of steps from the start position of the goniometer. The measured value is then compared to the theoretical shift values given by (5-5),

$$d_{theo} = \frac{\lambda}{\pi} \frac{1}{\sqrt{\cot(\theta_i)}\sqrt{\theta_d + |\delta_c|}}. \tag{5-5}$$

Solution for the three unknown parameters was performed using the Excel Solver™ function which implements the ***generalized reduction gradient nonlinear optimization code*** (GDR2). This method when applied to highly nonlinear functions requires a reasonably close approximation for a starting point and a scaled implementation of the unknown variables for good performance. Approximate starting parameters are obtained graphically by overlaying an

estimated model of divergence with the measured data. Centerline approximation is done first to align the shift graphs peaks positions. Then tilt offset is estimated visually.

Once close visual registration is attained the difference between measured and theoretical values are calculated for each sample point in the dataset and the error estimator is calculated using the least squares method given in (5-6). Solver is applied by attempting to minimize sigma by varying the three unknown parameters where sigma is given by (5-6),

$$\sigma = \sqrt{\frac{\sum_{1}^{n} \left( d_{meas} - d_{theo} \right)^2}{n}} . \qquad (5\text{-}6)$$

In some cases for large divergences the method will tend to diverge and manual convergence of the divergence angle is required. When this occurs the operator continually re-estimates divergence angle and converges individually on the tilt and critical angle only until a minimum sigma is obtained.

## *Conclusions:*

1. The divergence model for GH shift is experimentally confirmed.
2. Shift dependence on inverse square root of sum of divergence and alignment angle is experimentally observed and confirmed (see figures 5-13, 5-14, and 5-15).
3. Dispersion prediction of divergence model impulse response function is experimentally observed (see figure 5-10).
4. Mean edge position method of shift measurement is significantly more precise than the slope-intercept method in the data analysis.
5. Major sources of both systematic and random noise are identified and compensated or corrected.
6. Error analysis results are consistent with statistical theory.

# 6 - Summary and General Conclusions

The Goos-Hanchen effect has classically been limited by the ability of researchers to make measurements of sufficient accuracy to separate differing mathematical views of the phenomena. Likewise, the practical deployment of the physical effect has met with only limited success and is not in general competitive with alternate methods of better accuracy.

The main reason for this deficiency lies in the very small nature of the shift effect and the limitations of measuring devices to accurately resolve the dimensions involved. At operating wavelengths in the visible, the shift of a .001 radian divergence source is on the order of 5-6 microns. Prior practice was to produce multiple reflection shifts and manually measured the aggregate shift. In this work we have demonstrated the value of modern image processing in permitting more accurate measurements of the small dimensions involved in a single reflection shift and have attained shift resolutions on the order of 50-100 nanometers.

In this work we have studied the major controlling factors in amplification of the Goos-Hanchen shift, i.e. source divergence and ratio of refractive indices, and we conclude that modern apparatus under suitable control can significantly improve on the performance of prior experimenters. By identifying the dominant parameter of source collimation quality, we have shown mathematically that significant enhancement in attainable shifts can be achieved by proper source control. This level of control is now appropriate thanks in large measure to the advent of enhanced electronic ccd-imaging system sensitivities. Exploitation of this effect can

also be significantly enhanced by modern image processing methods and high density sampling methods.

Efficient experimental deployment involves a combination of these three areas of enhancement: source and grating control, digital imaging, and image processing. A well controlled source which previously might have lacked sufficient intensity for useable photographic processes is well suited for sensitive ccd-camera detection. Aperture shadow edge measurement which was previously limited by manual measurement methods can be greatly enhanced by high accuracy image processing methods and oversampling. Combining the technologies greatly enhances the sensitivities of modern experimental measurements. The ultimate limit of detectability then has two product terms: the sensitivity of shift to changes in optical properties and the resolvability of the image processing system, either of which possesses the potential for further improvement.

In this dissertation we have shown a mathematically closed form solution for the shift dispersion seen by collimated plane waves at internal reflection. We have shown the conditions under which these equations reduce to simple expression. We have reintroduced the concept of divergence, or angular spectrum distribution, and presented a simplified new model for explaining the spatial shift phenomena.

By introducing appropriately designed aperture methods we have found simple monotonic solutions for the shift effect observed by the shadow of the apertures. We have graphically

presented convolutions of the aperture effects and determined the theoretical intensity profiles which will be seen by an imaging system under direct observation.

Finally, we have shown that established edge detection methods using modern image processing can be optimized for our targets and extended by high density sampling and averaging methods to produce very high resolution results. The effect of combining these demonstrated methods is to significantly enhance the resolving power of single reflection experiments, thereby enabling straightforward scanning techniques for enhanced detection of critical angles and sensitivity to variations in refractive index.

Experimentally, we have demonstrated the dispersion effect and demonstrated the dependence of its measurement on the quality of focal control. We have also demonstrated the dependence of shift on the inverse square of the sum of divergence angle and alignment angle.

Analytically, we have found that the best results are obtained when experimental configurations permit multi-line sampling with shift averaging. The line irregularities of the gratings cause large errors when sampled individually which can be compensated by taking averages of multiple lines. This method produces viable results when rays are parallel as well as slightly divergent. In the former case a noticeable drop-off in shift magnitude occurs near the critical angle. In the latter case the drop-off can be reduced if the angular spread at the grating is less than the divergence angle of the source.

In all of the cases studied so far, we have found that maintaining adequate illumination strength at the grating is essential to minimizing both diffraction effects and imager noise. In the CCD camera, low light levels require activation of the automatic gain control (AGC) feature and significantly decrease the signal to noise ration of the imager.

### *Future efforts*

In this effort, we have demonstrated a fundamental model which simplifies attempts to describe the behavior of the GH shift phenomena near critical angle. The experiment evidence presented is basic and sound but not sufficient to deploy as a practical tool for high accuracy measurements.

We hope to continue these studies and eventually deploy precision measurement devices which exploit our methods. This effort will require more rigid and stable physical structures as well as automated scanning equipment. Both of these together can reduce noise and provide a higher consistency of readings. Additional improvements with better light sources are also possible. Finally, improvements in collimation and available light are indicated.

The experimental findings of this work suggest several directions for future investigation. The nature of the shift drop-off near critical angle for parallel rays warrants further study. Performance of the system with and without pinhole apertures will also be studied to determine the effectiveness of pinhole filtering in reducing divergence and attaining uniform spot sources. Variations in angular spread at the grating can be tested by uniform translation of the focusing lens and pinhole. This will shed additional light on the behavior of the line averaging

nonlinearities which occur near critical angle. The focusing lens to pinhole distance will be held constant in these tests to remove effects from changes in divergence.

Finally, physical improvements will be required to the mechanical setup of the apparatus to improve reliability of the overall system. Data collection can also be improved through implementation of automated scanning and focus control mechanisms.

# 7. References


1. I. Newton, *Opticks* (Dover, New York, 1952).
2. F. Goos and H. Hanchen, Ann Physik, 1, 333 (1947).
3. K. Artmann, Ann. Physik, "Calculation of Side Shift of Totally Reflected Beams," 2, 87 (1948).
4. H. Lotsch, "Reflection and Refraction of a Beam of Light at a Plane Interface," J. Opt. Soc. Am., 58 (4), 551 (1968).
5. P. Debye, Ann. Physik (4) 30,755 (1909).
6. J. Picht, Ann. Physik (5) 3, 433 (1929).
7. J. Agudin, "Time Delay of Scattering Processes," Physical Review, 171 (5), 1385 (1968).
8. R. H. Renard, "Total Reflection: A new Evaluation of the Goos-Hanchen Shift," J. Opt. Soc. Am., 54 (10), 1190 (1964).
9. B. Horowitz and T. Tamir, "Lateral Displacement of a Light Beam at a Dielectric Interface," J. Opt. Soc. Am., 61 (5), 586 (1971).
10. L. de Broglie and J. Vigier, "Photon Mass and New Experimental Results on Longitudinal Displacements of Laser Beams near Total Reflection," Physical Review Lett., 28 (15), 1001 (1972).
11. Y. Antar and W. Boerner, "Gaussian Beam Interaction with a Planar Dielectric Interface," Canadian Journal of Physics, 52, 962 (1974).
12. T. Tamir and H. Bertoni, "Lateral Displacement of Optical Beams at Multilayered and Periodic Structures," J. Opt. Soc. Am., 61 (10), 1397 (1971).
13. O. de Beauregard and C. Imbert, Physical Review D, 7 (12), 3555 (1973).

14. M. Green, P. Kirby and R.S. Timsit, “Experimental Results on the Longitudinal Displacement of Light Beams near Total Reflection,” Physics Letters, 45A, 3 (1973).
15. S. Kozaki and K. Kimura, “Wave Path of a Gaussian Beam in an Inhomogeneous Medium,” J. Opt. Soc. Am., 66 (1), 63 (1976).
16. A. Puri, D. Pattanayak, and J. Birman, “Resonance Effects on Total Internal Reflection and Lateral (Goos-Hanchen) Beam Displacement at the Interface between Nonlocal and Local Dielectric,” Physical Review B, 28 (10), 5877 (1983).
17. A. Puri and J. Birman, “Goos-Hanchen Beam Shift at Total Internal Reflection with Application to Spatially Dispersive Media,” J. Opt. Soc. Am. A, 3 (4), 543 (1986).
18. O. de Beauregard and C. Imbert, “Quantized Longitudinal and Transverse Shifts Associated with Total Internal Reflection,” Physical Review D, 7(12) (1973).
19. M. McGuirk and C.K. Carniglia, “An Angular Spectrum Representation Approach to the Goos-Hanchen Shift,” J. Opt. Soc. Am., 67 (1), 103 (1977).
20. S. Kozaki and H. Sakurai, “Characteristics of a Gaussian Beam at a Dielectric Interface,” J. Opt. Soc. Am., 68 (4), 508 (1978).
21. T. Tamir, “Nonspecular Phenomena in Beam Fields Reflected by Multilayered Media,” J. Opt. Soc. Am. A, 3 (4), 558 (1986).
22. F. Brentenaker, A Le Floch, and L. Dutriaux, Physical Review Letters, 68 (7), 931 (1992).
23. I.J. Singh and V.P. Nayyar, “Lateral Displacement of a Light Beam at a Ferrite Interface,” J. Appl. Phys.,69 (11), 7820 (1991).
24. R. Guther and B.H. Kleemann, Journal of Modern Optics, “Shift and Shape of Grating Diffracted Beams,” 45 (7), 1375 (1998).

25. R. Guther, B.H. Kleeman, J. Elschner, and G. Schmidt, "Determination of Longitudinal and Transverse Shifts of Three-Dimensional Gaussian Beam Reflected at a Grating near an Anomaly," Journal of Modern Optics, 49 (11), 1785 (2002).
26. P.R. Berman, "Goos-Hanchen shift in negatively refractive media," Physical Review E, 66 (2002)
27. X. Yin, L. Hesselink, Z. Liu, N. Fang, and X. Zhang, "Large Positive and Negative Lateral Optical Beam Displacements due to Surface Plasmon Resonance," Appl. Phys. Lett. Amer, 85, 372 (2004)
28. R. Micheletto, Y. Kawakami, K. Hamamoto, and S. Kawai, Opt. Lett., 31, 205 (2006)
29. J. Xu, Z. Fang, A. Malcolm, and H. Wang, "A Robust Close-Range Photogrammetric System for Industrial Metrology," Seventh Intl. Conference on Control, Automation, Robotics, and Vision. Pp 114-119, (2002).
30. K.W. Wong and W. Ho, Photogrammetric Engineering and Remote Sensing, 52(1) (1986), pp 67-74.
31. Kisworo, Venkatesh, and West, "Modeling Edges at Subpixel Accuracy Using the Local Energy Approach", IEEE Transactions on Pattern Analysis and Machine Intelligence, 16 (4), 405, (1994).
32. J. Canny, IEEE Trans on Pattern Analysis and Machine Vision, (8), 679-698, (1986).
33. M. Petrou and J. Kitler, "Optimal Edge Detectors for Ramp Edges", IEEE Transactions on Pattern Analysis and Machine Intelligence, 13 (5), 483 (1991).
34. Demigny, Lorca, and Kessal, "Evaluation of Edge Detectors Performances with a Discrete Expression of Canny's Criteria", Proceedings of International Conference on Image Processing, 2, 169, (1995).

35. Demigny and Kamle, “A Discrete Expression of Canny’s Criteria for Step Edge Detector Performances Evaluation”, IEEE Transactions on Pattern Analysis and Machine Intelligence, 19 (11), 1199, (1997).
36. Shi and Ward, “Canny Based Image Expansion”, International Conference on Circuits and Systems, Vol 1, 785, (2002).
37. Demigny, “On Optimal Linear Filtering foe Edge Detection”, IEEE Transactions on Image Processing, 11 (7), 728, (2002).
38. C.K.Lee, W.C. So, Proceedings of the International Conference on Industrial Electronics, Control, Instrumentation, and Automation, 1992. “Power Electronics and Motion Control”., Vol. 2, 710-715, (1992).
39. I. Popovici and W. Withers, IEEE Transactions on Pattern Analysis and Machine Intelligence, 28 (4), 637, (2006).
40. A.P. Reeves, M.L. Akey, and O.R. Mitchell, “A Moment Based Two-Dimensional Edge Operator,” Proceedings of IEEE CS Symposium, Computer Vision and Pattern Recognition, pp 312-317, (1983).
41. K. Ohtani and M. Baba, “A Fast Edge Location Measurement with Subpixel Accuracy Using a CCD Image,” IEEE Instrumentation and Measurement Technology Conference, 2087, (2001).
42. Y. Li, Y. Young and J. Magerl, “Subpixel Edge Detection and Estimation with a Microprocessor-Controlled Line Scan Camera,” IEEE Transactions on Industrial Electronics, 35 (1), 105, (1988).
43. J.D. Jackson, Classical Electrodynamics, (John Wiley and Sons, New York 3rd ed., (1999).

44. G.J. Troup, J.L.A. Francey, R.G. Turner, an A. Tirkel, , Phys. Rev. Lett, 28, 1540-1541, (1972)

45. M. Ben-Ezra, A. Zomet, and S.K. Nayar, "Video Super-resolution Using Controlled Subpixel Detector Shifts," IEEE Transactions on Pattern Analysis and Machine Intelligence, 27 (6), 977, (2005).

46. Lee and So, "A Fast Edge Detector with Subpixel Accuracy", Proceedings of the International Conference on Industrial Electronics, Control Instrumentation, and Automation, "Power Electronics and Motion Control", Vol. 2, 710, (1992).

47. C.V. Fragstein, Ann. Physik, 4, 271 (1949).

48. P. Bao, L. Zhang, and X. Wu, "Canny Edge Detection Enhancement by Scale Multiplication," IEEE Transactions on Pattern Analysis and Machine Intelligence, 27 (9), 1485, (2005).

49. J. Gray and A. Puri, "Quantitative Method for Measurement of the Goos-Hanchen Effect Based on Source Divergence Considerations", Physical Review A, 75, 063826-1-8 (2007).

50. J. Gray, "Exploiting Sub-pixel Edge Detection Methods with High Density Sampling to Provide .001 Pixels Rigid Target Localization", Proceedings SPIE International Society of Optical Engineering, 6579, 65790X (2007).

51. J. Gray and A. Puri, "Goos-Hanchen Divergence Model, Practical Measurement Considerations", submitted for publication.

# Vita

Jeffrey Gray was born in Dallas, Texas. He obtained a B.S. degree from the University of New Orleans in Electrical Engineering in 1984 and the M.S. degree from the University of New Orleans in Engineering in 1986. He has 19 years industrial experience as a Research Engineer in the areas of optical measurements technologies. He is currently an instructor in the Electrical Engineering department at the University of New Orleans.